DLR-IB-AT-BC-2021-257

Fan Noise Measurements of a Blisk Rotor at the Low Speed Fan Test Rig FloCon

Interner Bericht

Lukas Klähn
Luciano Caldas
Ulf Tapken

DLR Deutsches Zentrum für Luft- und Raumfahrt

Dokumenteigenschaften

Titel	Fan Noise Measurements of a Blisk Rotor at the Low Speed Fan Test Rig FloCon
Betreff	
Institut	Antriebstechnik
Erstellt von	Lukas Klähn
Beteiligte	Luciano Caldas, Ullf Tapken
Geprüft von	
Freigabe von	
Datum	22.03.2021
Version	1.0
Dateipfad	\\at-tra-terra\Documents\Berichte_Veroeffentlichungen_Konferenzen_AT-TRA\DLR_Interne_Berichte

Contents

1 Introduction

At the Engine Acoustics Department of the DLR-Institute of Propulsion Technology a new Blade Integrated Disk (Blisk) Rotor was implemented in the FloCon test rig. In this context a comprehensive experimental study was performed to determine the aerodynamic engine map as well as the acoustic characteristics at numerous operating points.

The first objective is the investigation of the influence of the aerodynamically optimized rotor on the Fan-performance and the acoustic characteristics. This is addressed by comparison with previous measurements with a similar experimental setup but a different rotor design by Tapken et al. [11] and with an accompanying PropNoise study.

This report however focusses on providing an extensive database as a reference for future measurements on the FloCon test rig and other low pressure test rigs. Several mode analysis techniques, that are used in the Engine Acoustics Department, are applied on the measurement data and the results are presented in this report.

The analyses that were done are not always completed in the sense, that some questions remained open and are mentioned in this report as suggestions for further studies and analyses at the end of each section.

2 Experimental Setup

In this section the test rig and the used instrumentation for the aerodynamic and acoustic measurements are described. Further information can be found in the manuals of the FloCon test rig [2, 1]. The measured operating points are briefly described.

2.1 Characteristics of the Test Rig

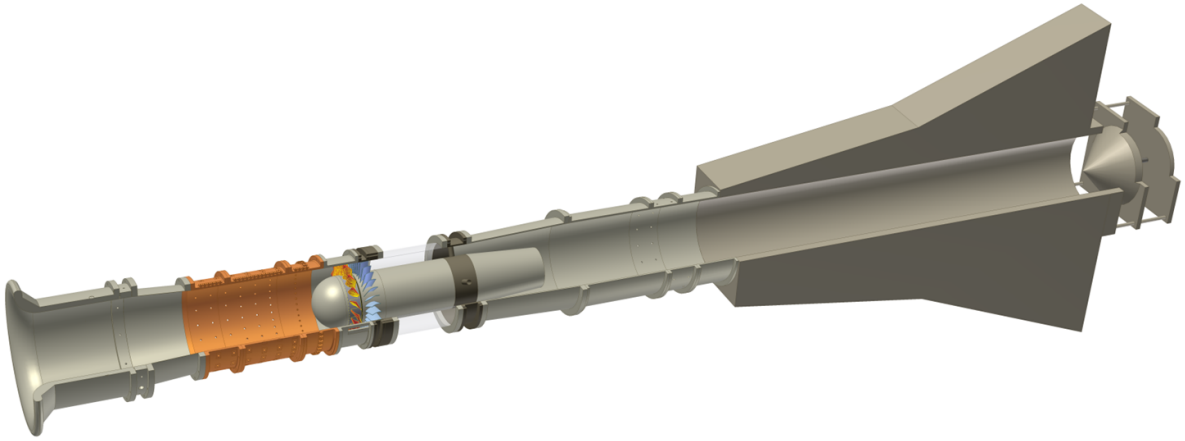

Figure 2.1: The FloCon test rig from left to right: Bellmouth, nozzle, inlet measurement section, rotor-stator stage, diffusor, outlet measurement section, anechoic outlet, throttle.

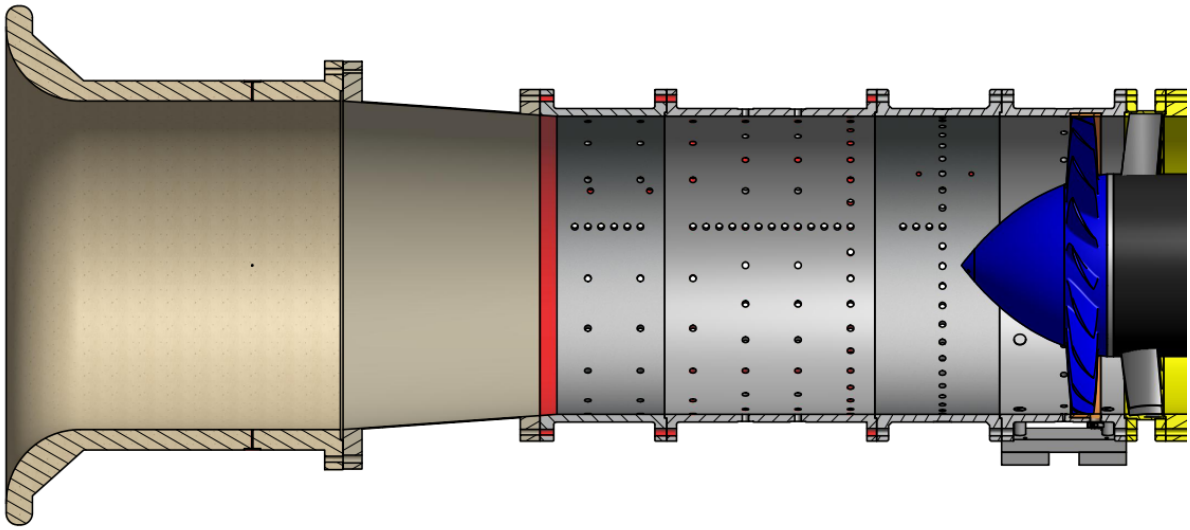

Figure 2.2: Detailed illustration of the inlet section.

A cylindrical coordinate system with origin in the rotor plane is used. The axial coordinate x is pointing in positive mean flow direction and for the circumferential coordinate θ the 'right hand rule' is applied. In this coordinate system the rotor is spinning in negative θ direction, see also figure 2.3.

Figure 2.3: Implemented rotor without the casing

2.2 Acoustic Instrumentation

The Acoustic instrumentation is depicted in figure 2.4. The respective ring arrays are equipped accordingly to the defined coordinate system. The exact positions are saved in an Excel sheet.

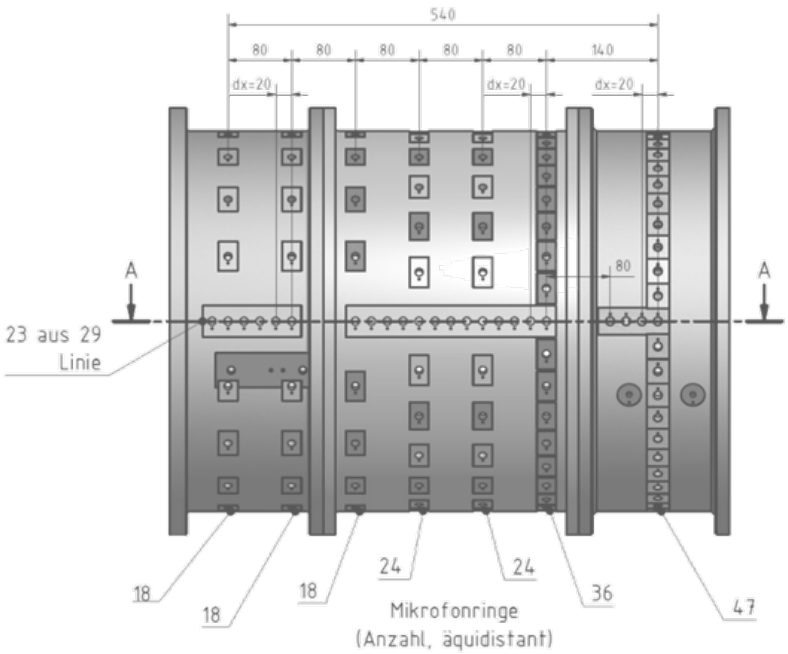

Figure 2.4: The microphone array consists of six rings numerated from left to right. Ring 1, ring 2 and ring 3 consist of 18 microphones, ring 4 and ring 5 consist of 24 microphones and ring 6 consists of 36 microphones that are uniformly distributed in azimuthal direction respectively. Additionally, a line array is used with 23 uniformly spaced microphones, except for two gaps caused by the ducts flanges.

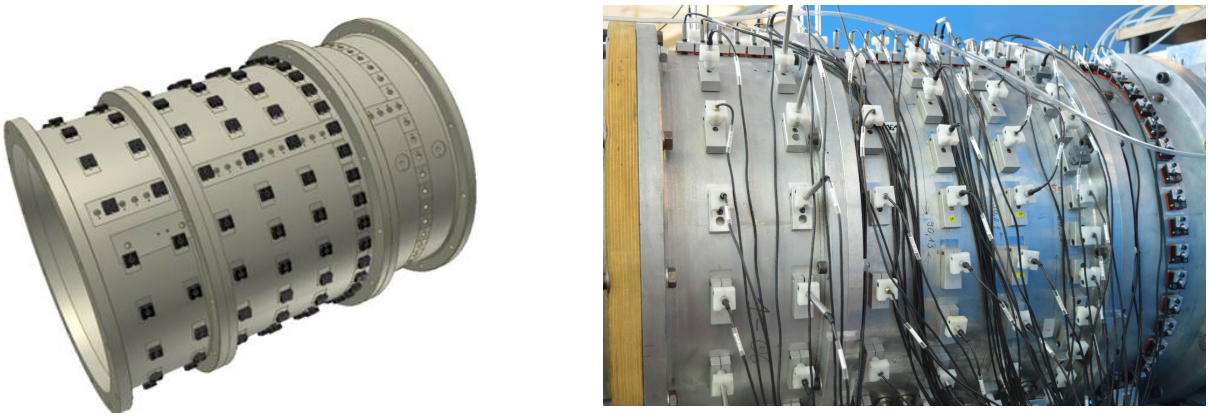

Figure 2.5: The microphone array that was used for the radial mode analysis.

2.3 Operating Points

In figure 2.6 the measured performance map of the fan is shown. The operating points are specified in more detail in tables A.1 and A.2. The calculation of the aerodynamic parameters is described in [1], a quick overview is given in figure A.1.

Flow coefficient ϕ and fan loading ψ are non-dimensional values of the mass flow and

pressure rise. Under idealized conditions the ϕ-ψ graph is independent of the rotor speed:

$$\phi = \frac{M_{\text{in}}}{M_{\text{tip}}} \frac{R_{\text{in}}^2}{R_{\text{R}}^2}\,, \tag{2.1}$$

$$\psi = \frac{\Pi - 1}{\frac{1}{2}\,\kappa\, M_{\text{tip}}^2}\,. \tag{2.2}$$

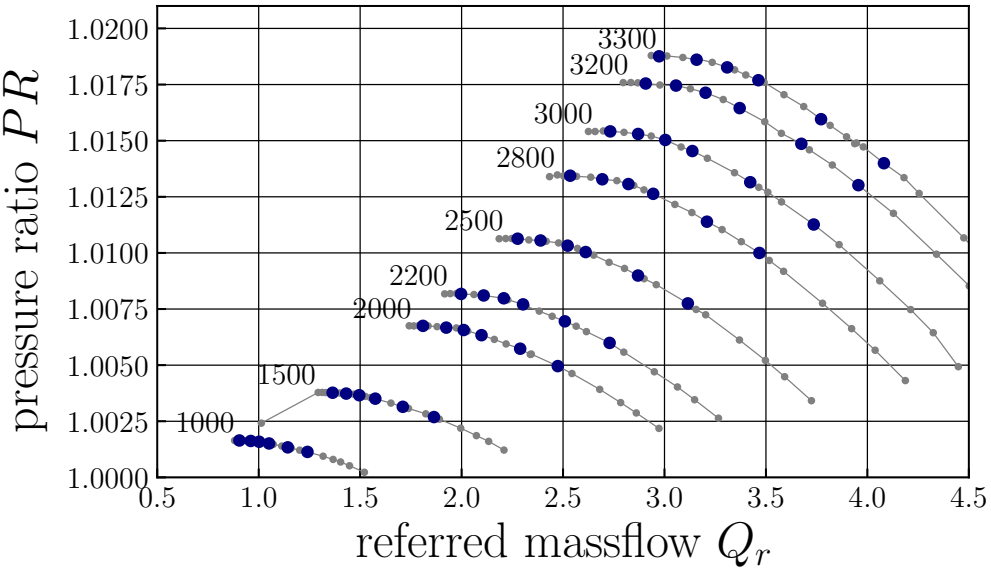

Figure 2.6: Operating points in the domain of pressure rise and reduced mass flow. The operating points where acoustic measurements were performed are marked in blue.

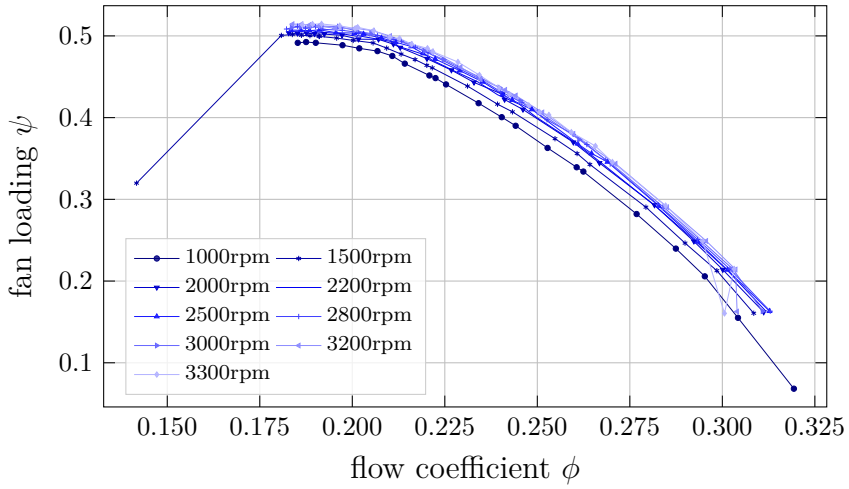

Figure 2.7: Operating points in the domain of fan loading and flow coefficient. This Graph is characteristic for the Fan and is in theory independent of the rotor speed. Deviation occur however at low speeds due to a smaller Reynolds number.

3 Theoretical Background

3.1 Description of Mode Propagation in Hard-Walled Annular Flow Ducts

As described comprehensively in [10], the sound field in a hard walled duct with uniform axial mean flow can be represented as a superposition of acoustic modes of the form:

$$p\left(x,r,\theta,t\right) = \sum_{m=-\infty}^{\infty}\sum_{n=0}^{\infty}\left(A_{mn}^{+}\ e^{jk_{mn}^{+}x} + A_{mn}^{-}\ e^{jk_{mn}^{-}x}\right)\ f_{mn}(r)\ e^{jm\theta}\ e^{-\omega t}. \tag{3.1}$$

With p denoting the acoustic pressure, (x,r,θ) the cylindrical coordinates and t the time. m and n are the azimuthal and radial mode orders respectively. $A_{mn}^{\pm}$ is the modal amplitude, the sign denotes the direction of propagation, downstream being marked with a "+" and upstream with a "-" respectively. The axial wave number is $k_{mn}^{\pm}$ and the radial eigenfunction is $f_{mn}(r)$. In the following the harmonic time dependency is omitted. The axial wavenumber in an uniform axial mean flow is:

$$k_{mn}^{\pm} = \frac{k}{1-M-x^2}\left(-M_x \pm \sqrt{1-(1-M_x^2)\frac{\sigma_{mn}^2}{(kR)^2}}\right), \tag{3.2}$$

with σ_{mn} being the Eigenvalue which is found by adjusting the radial eigenfunktion to the boundary condition of a hard walled duct [10]. By radial mode analysis a solution of the radial mode amplitudes $A_{mn}^{\pm}$ is found. The radial mode amplitudes are determined by solving equation (3.1) in vector notation:

$$\boldsymbol{p} = \boldsymbol{W}\cdot\boldsymbol{a}\,, \tag{3.3}$$

with $\boldsymbol{p}$ the vector of microphone signals, $\boldsymbol{W}$ the Transfer Matrix and $\boldsymbol{a}$ the vector of the radial mode amplitudes. Alternatively equation (3.1) can be simplified for the azimuthal mode analysis (AMA):

$$p\left(x,r,\theta\right) = \sum_{m=-\infty}^{\infty} A_m\left(x,r\right)\ e^{jm\theta}\,, \tag{3.4}$$

$$\boldsymbol{p} = \boldsymbol{W}_{\mathrm{AMA}}\cdot\boldsymbol{a}_{\mathrm{AMA}}\,, \tag{3.5}$$

$$A_m\left(x,r\right) = \sum_{n=0}^{\infty} A_{mn}^{+}\ e^{jk_{mn}^{+}x} + A_{mn}^{-}\ e^{jk_{mn}^{-}x}\,. \tag{3.6}$$

The least squares fit solutions of equations (3.3) and (3.5) are calculated with the pseudo-inverse of the transfer matrix:

$$\boldsymbol{W}^{\dagger} = \left[\boldsymbol{W}^{H}\cdot\boldsymbol{W}\right]^{-1}\cdot\boldsymbol{W}^{H}. \tag{3.7}$$

This method is sufficient, if the modes are fully correlated. If the modes are however not fully correlated, the cross spectral matrix of the mode amplitudes $\boldsymbol{S}_{aa}$ can be calculated from the cross spectral matrix of the microphone signals $\boldsymbol{S}_{pp}$ [3]:

$$\boldsymbol{S}_{pp} = \boldsymbol{W}\cdot\boldsymbol{S}_{aa}\cdot\boldsymbol{W}^{H}, \tag{3.8}$$

$$\boldsymbol{S}_{aa} = \boldsymbol{W}^{\dagger}\cdot\boldsymbol{S}_{pp}\cdot\left[\boldsymbol{W}^{\dagger}\right]^{H}. \tag{3.9}$$

3.2 Cyclostationary Mode Analysis

After the signal is resampled, the signal is transformed to the frequency domain via FFT. For the FFT a block length of $L_{\text{block}} = 16384$ was used, that corresponds exactly to 16 rotor revolutions. A rectangle window and no overlap is used, because the tones of interest exactly match integer multiples of the sample width. In the standard procedure, the FFT is performed for each block, and the auto power spectral density is calculated as a mean over all results. To calculate the cyclostationary component CyS1, the signal is averaged in the time domain, before the FFT is performed. For the CyS2 components, the average is subtracted from the time signal before the FFT.

$$\begin{aligned} S_{pp} &= \textstyle\sum_i \frac{p_i\, {p_i}^*}{N_{\text{blocks}}} && \text{, with} && p_i &= FFT(\tilde{p}_i)\,, \\ S_{pp,\text{CyS1}} &= p_{\text{CyS1}}\, {p_{\text{CyS1}}}^* && \text{, with} && p_{\text{CyS1}} &= FFT\left(\textstyle\sum_i \frac{\tilde{p}_i}{N_{\text{blocks}}}\right)\,, \\ S_{pp,\text{CyS2}} &= \textstyle\sum_i \frac{p_{\text{CyS2},i}\, {p_{\text{CyS2},i}}^*}{N_{\text{blocks}}} && \text{, with} && p_{\text{CyS2},i} &= FFT\left(\tilde{p}_i - \textstyle\sum_i \frac{\tilde{p}_i}{N_{\text{blocks}}}\right)\,. \end{aligned} \tag{3.10}$$

Here $\tilde{p}_i$ denotes one block of the resampled time signal and N_{blocks} is the number of blocks. Similarly the cross spectra S_{pq} for each combination of microphone positions are calculated.

4 Acoustic Characteristics of the FloCon Test Rig

4.1 Cut-On Modes

The number of analyzable modes depends on the used method. Using the Full Sensor Array (FSA) method for the radial mode analysis (RMA), the maximum frequency is at about $f_{max} = 2000\,\text{Hz}$ [11]. In this frequency range modes of azimuthal order up to $m = 6$ are propagating and the maximum radial order is $n = 2$.
Using the azimuthal mode analysis (AMA) with ring 6 up to 36 azimuthal mode orders can be separated. The cut-on frequency of the modes with order $(m, n) = (\pm 18, 0)$ is about $f_{\pm 18,0} \approx 4830\,\text{Hz}$. Above this frequency aliasing effects occur and this is therefore the maximum frequency for the AMA method.

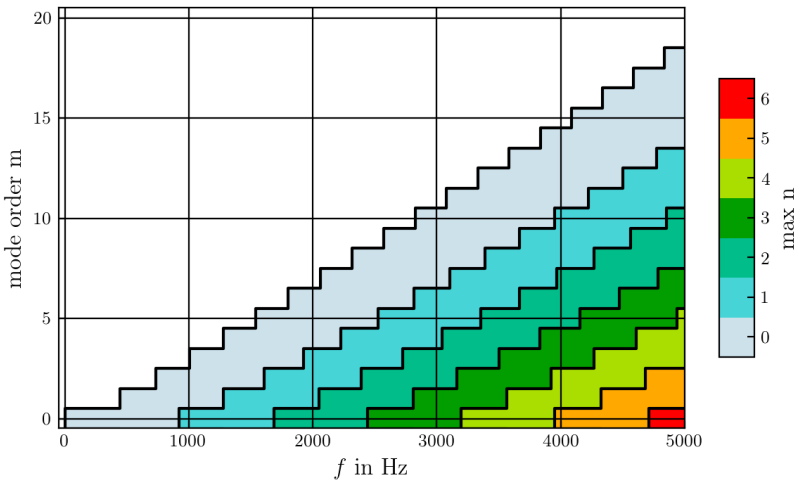

Figure 4.1: Cut-on frequencies in the microphone array section. As no swirl is assumed, the cut-on frequencies of negative m are omitted, as they are identical to the positive counterpart.

4.2 Rotor-Stator Interaction Modes

The fan stage consists of the Blisk rotor with $B = 18$ Blades and a stator with $V = 32$ Vanes. Due to the negative spinning direction of the Rotor, the Tyler-Sofrin modes [12] are

$$m = -hB \pm nV \quad , n \in \mathbb{N}\,. \tag{4.1}$$

For the first harmonic ($h = 1$) of the blade passing frequency (BPF) this results in a cut-off design for all operating points, while for $h = 2$ the azimuthal order $m = -4$ is excited by the rotor-stator interaction. The Tyler-Sofrin modes are summarized in table 4.1.

h	1	2	3	4	5
m	14	-4	10	-8	6
f_c in Hz	3834	1276	2825	2316	1800

Table 4.1: Tyler-Sofrin modes with respective cut-on frequency for the operating point 3200E

4.3 Inflow Control Device

In the experiment a simplified inflow control device (ICD) was attached to the inlet, as depicted in figure 4.2. Oertwig [7] showed how an existing ICD could be improved. The used ICD is an advanced version, based on the work of Oertwig [7]. The turbulence intensity and the non stationary and non homogeneous inflow distortions are reduced significantly compared to the baseline measurement without ICD. However, the boundary layer is still non homogeneous in circumferential direction. But the flow field including the inhomogeneous boundary layer are more stationary in time. Thus a new ICD was designed by Caldas et al. [4] for further experiments.

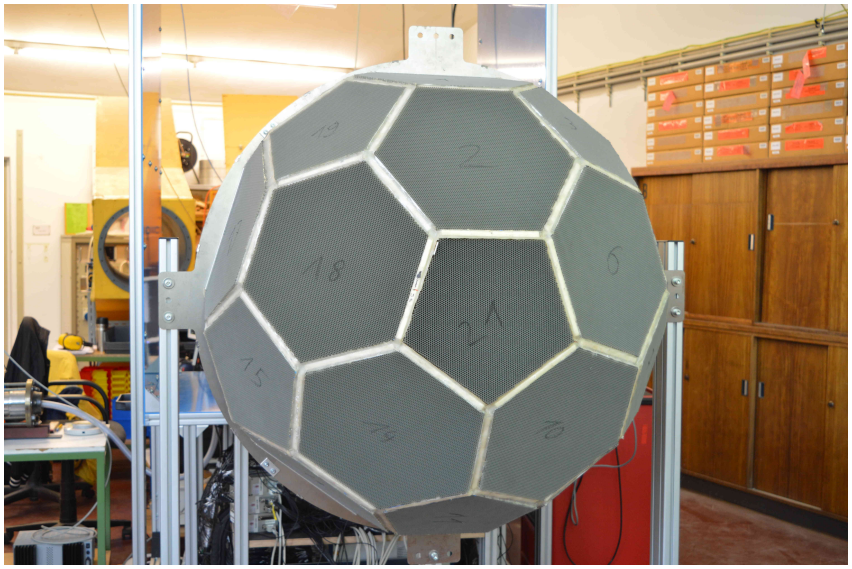

Figure 4.2: Simplified TCS

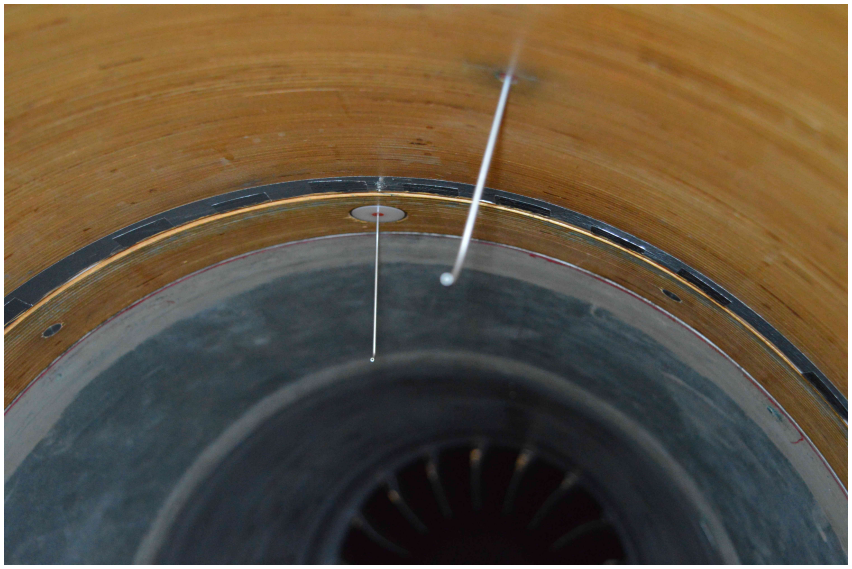

Figure 4.3: Intrusive pressure measurement with Pitot tubes upstream of the fan. The resulting inflow distortion might affect the acoustic sources.

4.4 Assessment of the Analysis Quality

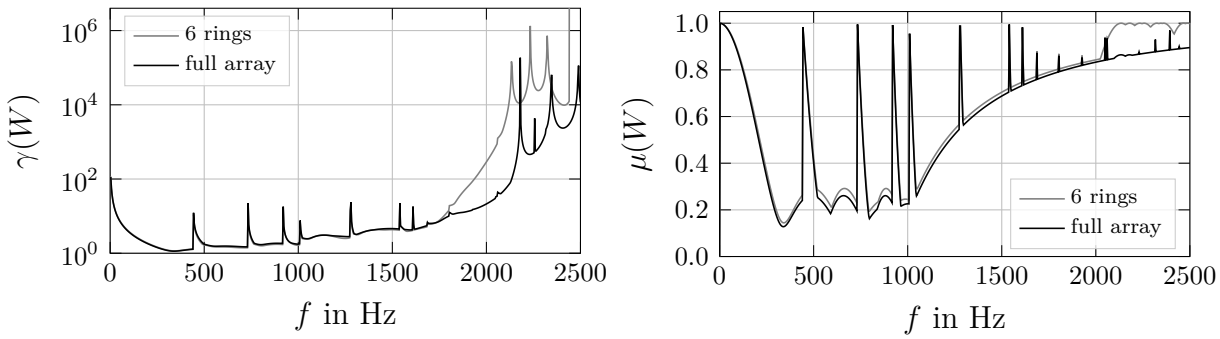

(a) Condition Number

(b) Mutual Coherence

Figure 4.4: Assessment of the analysis quality

The Ring Array with circumferentially uniform distributed sensors is the optimal Array for the azimuthal mode analysis, as long as the number of cut-on modes does not exceed the number of sensor positions. The optimal axial distance of the sensors is not that straightforward to find, but it can be optimized by minimizing the condition Number $\gamma(\boldsymbol{W})$ or with simulated measurements [10]. In figure 4.4a the condition number is shown for the full array (with the line array) in black and for the 6 ring arrays combined in grey respectively. Another common measure for microphone arrays is the mutual coherence of the transfer matrix $\mu(\boldsymbol{W})$, that is shown in figure 4.4b. The condition number of both arrays is nearly identical up to about 1700 Hz. Above that frequency, the condition number of the reduced array without the line (6 rings) raises significantly higher than for the full array and jumps to extremely high values at the cut-on Frequency of the mode $(0, 3)$ at about 2440 Hz. The mutual coherence is rather high at low frequencies and at the cut-on frequencies, where the axial wave numbers are very small and the phase

difference is too small for a clear separation of down- and upstream propagating modes of the same order. At about 2000 Hz the axial Distance of the Rings is of the same order is half the axial wavelength of the plane wave and the mutual coherence rises to the Value 1. The full array, including the line array, has a slightly lower mutual coherence, which doesn't raise to 1 at 2000 Hz because in the line array the axial distance is a fourth of the axial ring distances. Including the line array into the analysis is expected to increase the frequency range of the radial mode analysis with the FSA method. For the line array, the limitation due to the wavelength at higher frequencies is four times higher. However, the most significant improvement of the condition number is observed in the frequency range between 1700 Hz and 2200 Hz. Further analysis tools using the line array, like the CAAS method, can be applied to improve the analysis quality and the frequency range [11].
A more reliable error estimate is determined by a Monte-Carlo study of simulated measurements. With the Monte Carlo study a measure of how much the noise in the microphone signals is amplified in the mode analysis process is calculated [10]. From the simulated measurements the standard deviation[1]of the mode amplitudes can be estimated. The standard deviation is normalized with the uncertainty of the sound pressure vector:

$$\hat{\sigma}_p(A_{mn}^{\pm}) = \frac{1}{\sigma_{\text{noise}}} \sqrt{\frac{1}{N_{\text{sim}}-1} \sum_{i=0}^{N_{\text{sim}}-1} |A_{mn}^{\pm}[i] - A_{mn}^{\pm 0}|^2}\,, \tag{4.2}$$

$$\hat{\sigma}_p(A_{m}^{\pm}) = \sqrt{\sum_{n=0}^{N_n} \left(\hat{\sigma}_p(A_{mn}^{\pm})\right)^2}\,. \tag{4.3}$$

σ denotes the standard deviation, with the hat symbol indicating the estimator of the value. The index p indicates that in the procedure of the Monte-Carlo study noise is added to the simulated microphone signals. The procedure can be sketched as follows:

1. From an arbitrary synthetic mode amplitude vector with the entries $A_{mn}^{\pm 0}$ the sound pressure at the microphone positions is calculated with equation (3.3): $\boldsymbol{p}_0 = \boldsymbol{W} \cdot \boldsymbol{a}_0$.
2. To the sound pressure vector a normally distributed noise vector $\boldsymbol{n}[i]$ is added. The standards deviation of the noise Vector is σ_{noise}: $\boldsymbol{p}[i] = \boldsymbol{p}_0 + \sigma_{\text{noise}}\boldsymbol{n}[i]$.
3. The simulated mode analysis is performed with the pseudo inverse: $\boldsymbol{a}[i] = \boldsymbol{W}^{\dagger} \cdot \boldsymbol{p}[i]$, where the entries of $\boldsymbol{a}[i]$ are $A_{mn}^{\pm}[i]$.
4. Repeat steps 2. and 3. N_{sim} times.
5. Calculate the normalized standard deviation $\hat{\sigma}_p$.

Alternatively, the relative error can be calculated by a sensitivity analysis [9]. From equation (3.3) it follows that:

$$\frac{\partial \boldsymbol{a}}{\partial \boldsymbol{p}} = \boldsymbol{W}^{\dagger}\,. \tag{4.4}$$

[1]Additionally to the standard deviation Tapken [10] used the expression $\frac{1}{N_{\text{sim}}} \sum_{i=0}^{N_{\text{sim}}-1} \sqrt{\sum_{n=0}^{N_n} \left|A_{mn}^{\pm}[i] - A_{mn}^{\pm 0}\right|^2}$.

Let $\boldsymbol{w}_j^\dagger$ be the j-th column of the pseudo inverse $\boldsymbol{W}^\dagger$, such that the partial derivative of the mode amplitude vector is:

$$\frac{\partial \boldsymbol{a}}{\partial p_j} = \begin{bmatrix} \frac{\left[A_{mn}^{\pm}\right]_0}{\partial p_j} \\ \frac{\left[A_{mn}^{\pm}\right]_1}{\partial p_j} \\ \vdots \\ \frac{\left[A_{mn}^{\pm}\right]_{N_{Modes}-1}}{\partial p_j} \end{bmatrix} = \boldsymbol{w}_j^\dagger \,. \tag{4.5}$$

The standard deviation of the mode amplitudes with respect to the uncertainties in the microphone signals is then:

$$\sigma_p\left(A_m^{\pm}\right) = \sqrt{\sum_{n=0}^{N_n} \sum_{j=0}^{N_{\text{mic}}-1} \left(\frac{\partial A_{mn}^{\pm}}{\partial p_j}\right)^2}, \tag{4.6}$$

with p_j denoting the sound pressure measured at the j-th microphone position.

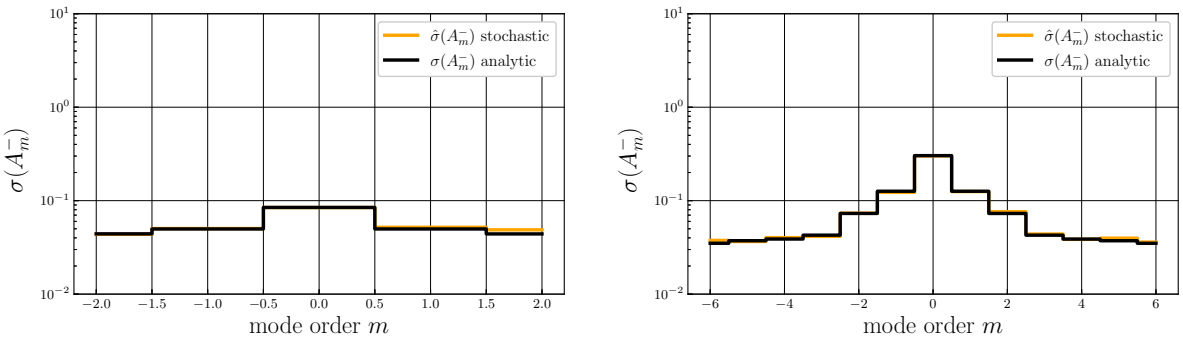

(a) 1 BPF (b) 2 BPF

Figure 4.5: Stochastic and analytic relative standard deviation of the azimuthal mode amplitudes. The Monte-Carlo study included 100 simulated measurements.

This sensitivity analysis was applied using the 6 ring arrays and using the full array, shown in the figures 4.6 and 4.7 respectively. As shown in figure 4.6, the relative error of the azimuthal order 0 is the most critical. For this mode the relative error is above 1, well below 2 kHz, when only the 6 ring arrays are used. In figure 4.7, the relative error of the full array is shown. The relative error of the azimuthal orders $m = \{-1, 0, 1\}$ raise to critically high values at virtually the same frequency of approximately 2100 Hz. The relative error of the azimuthal order 0 is still the highest at lower frequencies.
As these errors, at relative low frequencies are caused by a poor condition of the transfer matrix $\boldsymbol{W}$, the analysis can be improved by a regularized pseudo inverse of the transfer matrix [8]:

$$\boldsymbol{W}_{\text{reg}}{}^\dagger = \left[\boldsymbol{W}^H \cdot \boldsymbol{W} + \eta^2 \boldsymbol{I}\right]^{-1} \cdot \boldsymbol{W}^H. \tag{4.7}$$

Here η^2 denotes the regularization parameter .

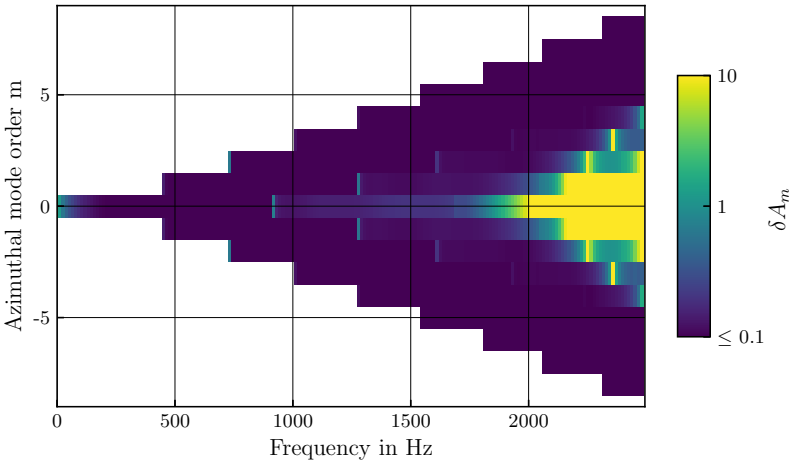

Figure 4.6: Analytically determined relative error up to 2.5 kHz with the 6 ring arrays.

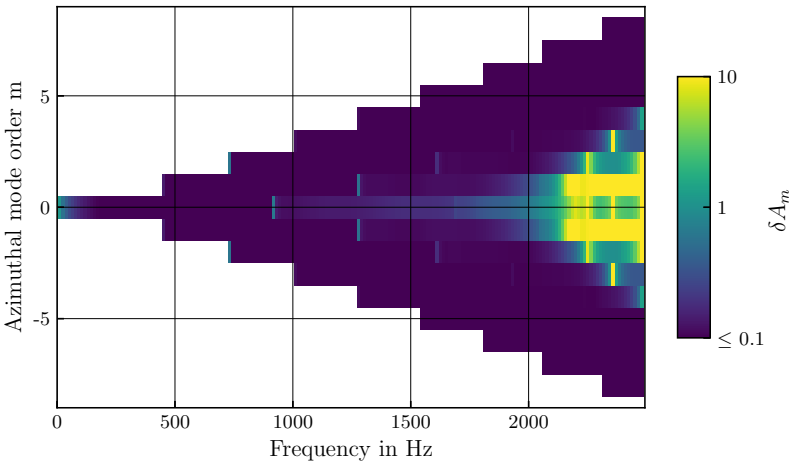

Figure 4.7: Analytically determined relative error up to 2.5 kHz with the full array.

Alternative to the sensitivity analysis, the relative error can be estimated with a Monte Carlo study where random noise is added to the microphone data and the stochastic standard deviation is calculated. With this approach the error can be calculated with the regularization included. In figure 4.8 the relative error using the full array is shown. The result converges with more simulated measurements to the result of the sensitivity approach.

In figure 4.9 the relative error using the full array and a regularized pseudo inverse is shown. The error is also at higher frequencies very small. It shall be noted, that the regularization indeed suppresses the noise, added to the microphone signals. But as the regularization parameter increases with higher frequencies, also the mapping onto the mode amplitudes is regularized and becomes underestimated.

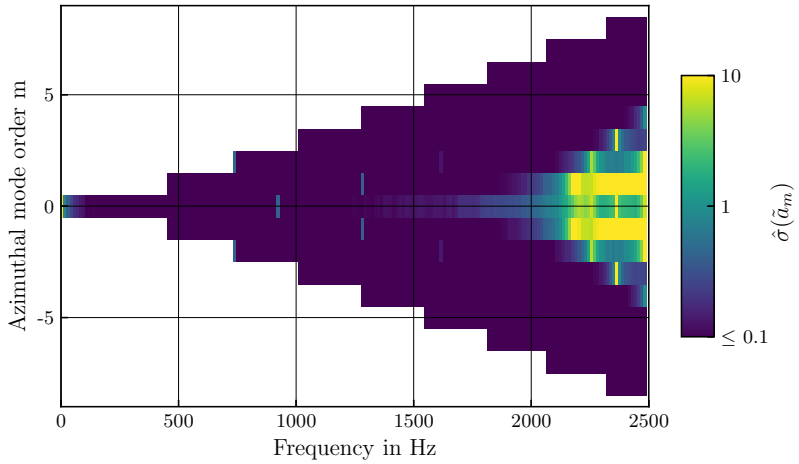

Figure 4.8: Estimated relative error of 100 simulated measurements up to 2.5 kHz with the full array.

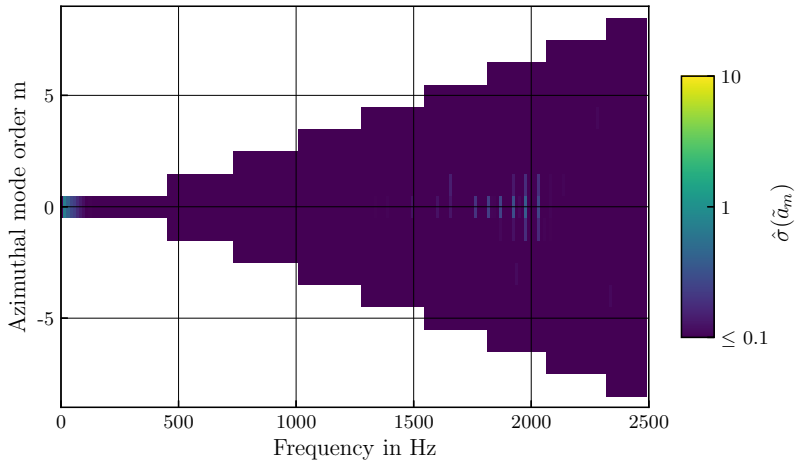

Figure 4.9: Estimated relative error of 100 simulated measurements up to 2.5 kHz with the full array and regularization.

Further work concerning the error and regularization of radial mode analysis must be done and could consider the residuum of the mapping and the regularization parameter η. Another open question is how the error of the broadband RMA method is correctly estimated.

5 Analysis of Sound Pressure Time Series

During the experiments, no Microphone was suspected to be defect. This was also confirmed by looking at the auto power spectral densities of all Microphones in figure 5.1. In a first step, the time signals were adaptively resampled to compensate for the rotor speed fluctuations. secondly, a cyclo stationary analysis was performed, to split the signal into pure rotor originated tones, and stochastic broadband noise.

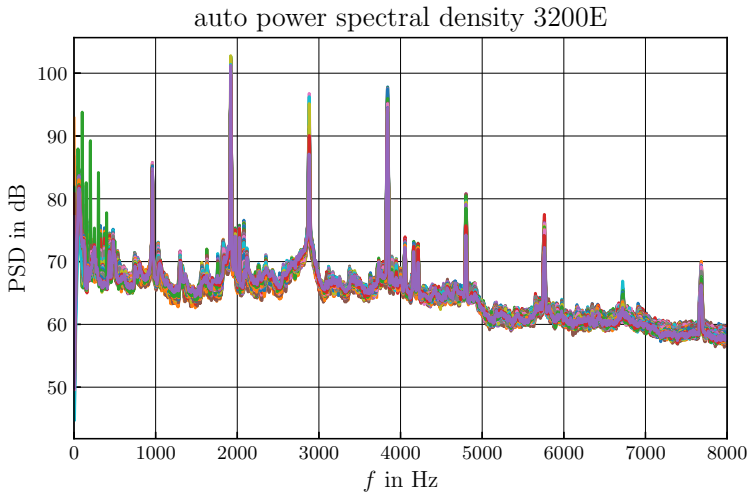

Figure 5.1: Auto power spectral densities of all microphones for the operating point 3200E.

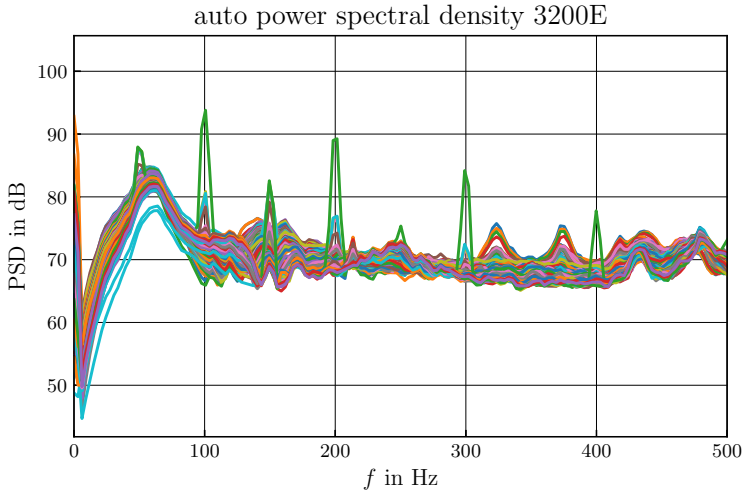

Figure 5.2: Auto power spectral densities of all microphones for the operating point 3200E. One Microphones shows relatively high amplitudes at 50 Hz and it's higher harmonics. This noise originates from the microphone power supply chain and is not rotor coherent. It is therefore filtered in the cyclostationary signal processing.

5.1 Adaptive Resampling

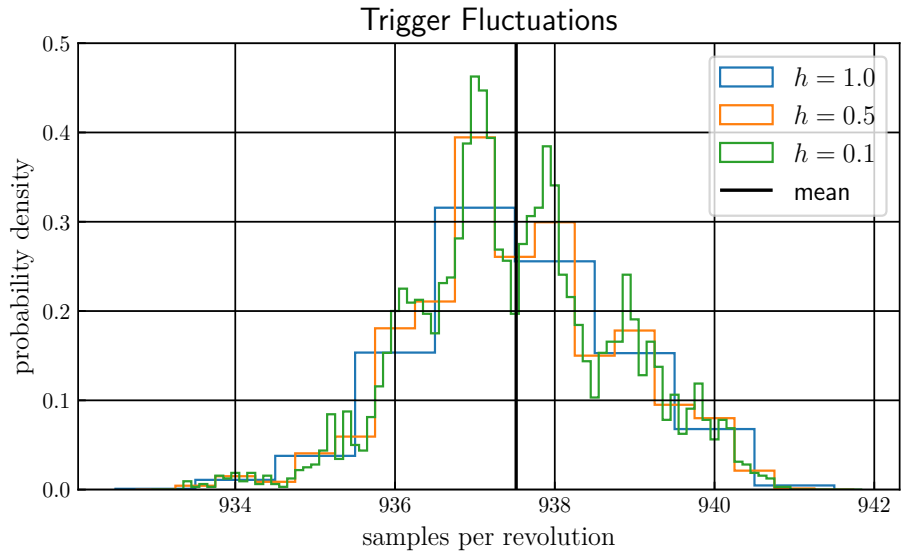

Figure 5.3: Probability density of the trigger fluctuations with different bin widths. The vertical line marks the mean number of samples per Revolution

The sampling frequency of the measurement rig was 50 000 Hz. At a rotor speed of 3200 RPM about 937.5 samples are recorded per revolution. The signal was adaptively resampled, such that the number of samples per revolution corresponds to the next higher power of 2, in this case $N_{\text{resamp}} = 1024$. Figures 5.3 and 5.4 show the rotor speed fluctuations in terms of samples per revolution.

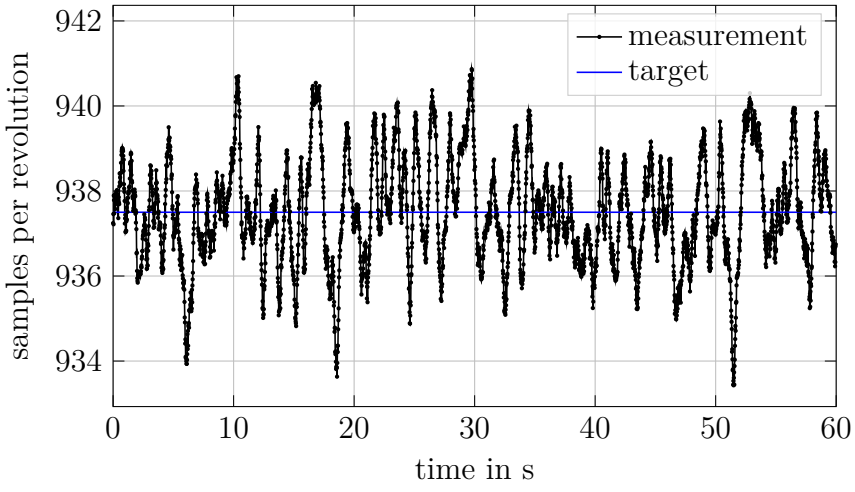

Figure 5.4: Linear interpolation of the number of samples per rotor revolution over the time. The motor control is constantly adjusting the shaft speed, resulting in the shown fluctuation around the target speed.

5.2 Evaluation of Signal-to-Noise Ratio

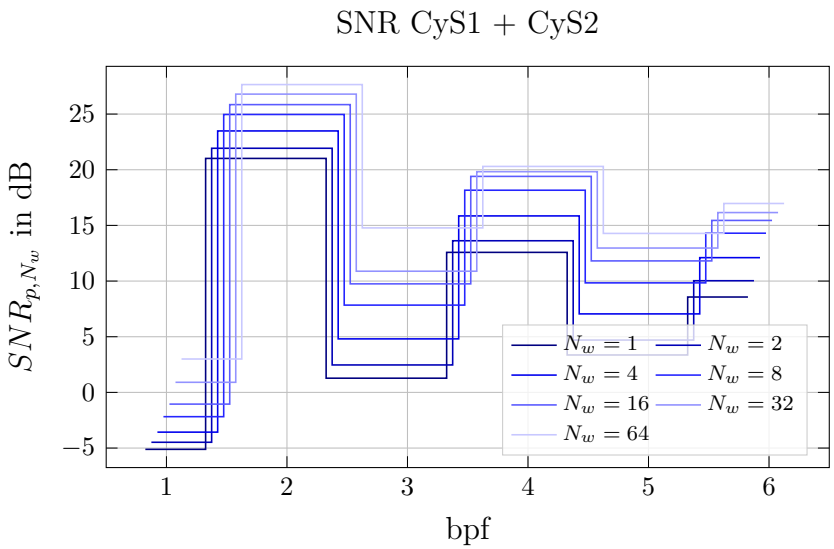

Figure 5.5: Signal to noise ratio for Measurement lengths

The error of the sound pressure amplitudes at the BPF and its higher harmonics can be expressed as a standard deviation between N_{meas} Measurements. Alternatively a long measurement signal can be divided into N_{meas} short measurements, that are treated as individual measurements, which was done here. From the Standard deviation the signal-to-noise ratio (SNR) calculated. The method is described by Tapken [10] For the SNR evaluation, different measurements lengths are used, that correspond to integer muiltiples of the FFT blocklength:

$$L_{\text{meas}} = N_w \cdot L_{\text{block}} \,, \tag{5.1}$$

with N_w the number of windows, or blocks per measurement. For the operating point 3200E, the resampled signal was divided into 199 blocks. In the SNR evaluation with only one block per measurement ($N_w = 1$) the standard deviation between 199 measurements is calculated. With $N_w = 64$ only 3 measurements are used to calculate the standard deviation. At the first BPF the Tyler-Sofrin mode is cut-off and the SNR is very small. This indicates high fluctuations in the source strength at this frequency. At the second bpf the Tyler-Sofrin mode is cut-on and the SNR is very high. This indicates a rather constant amplitude of the rotor stator interaction mode at this frequency.
In figure 5.5 the SNR is averaged over all microphones. In a further analysis the SNR may be calculated for each microphone individually. These values can the be used to estimate a modal SNR value.

5.3 Spectrogram

In this subsection the FFT windows for two selected microphones are analyzed. The used microphones are located at the two edges of the line array. The used operating point is 3200E.

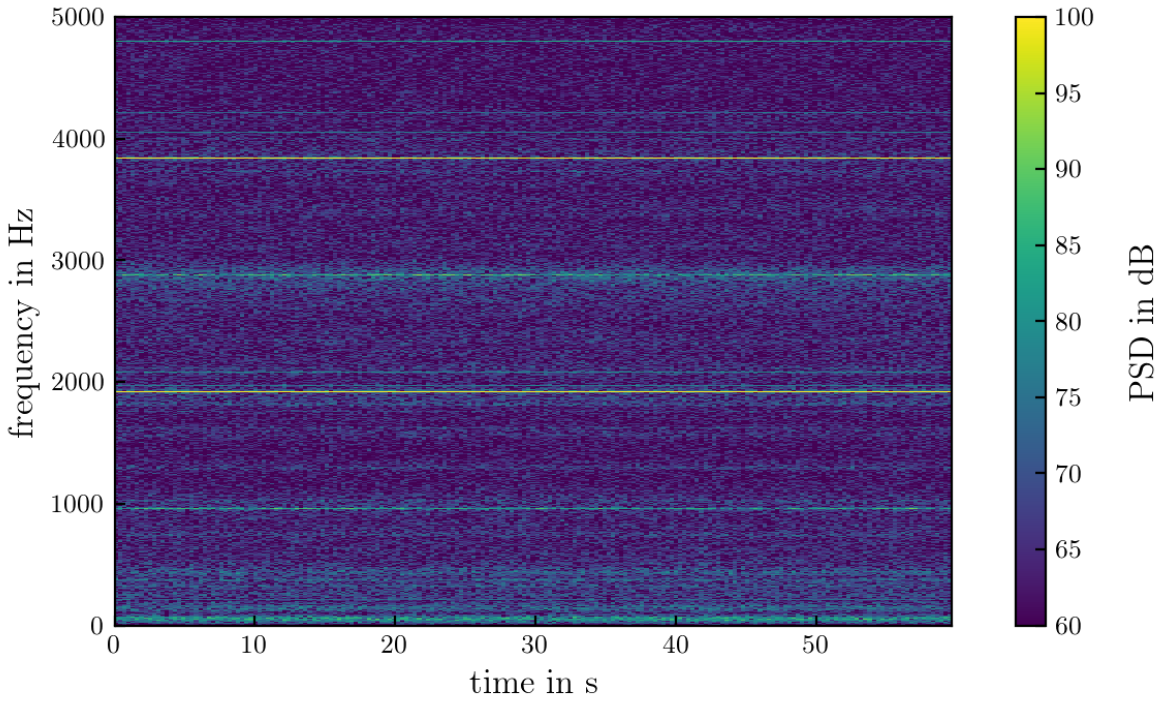

Figure 5.6: Spectrogram as power spectral density in dB resp. $^{20\,\mu Pa}/_{\sqrt{Hz}}$. Microphone closest to the rotor.

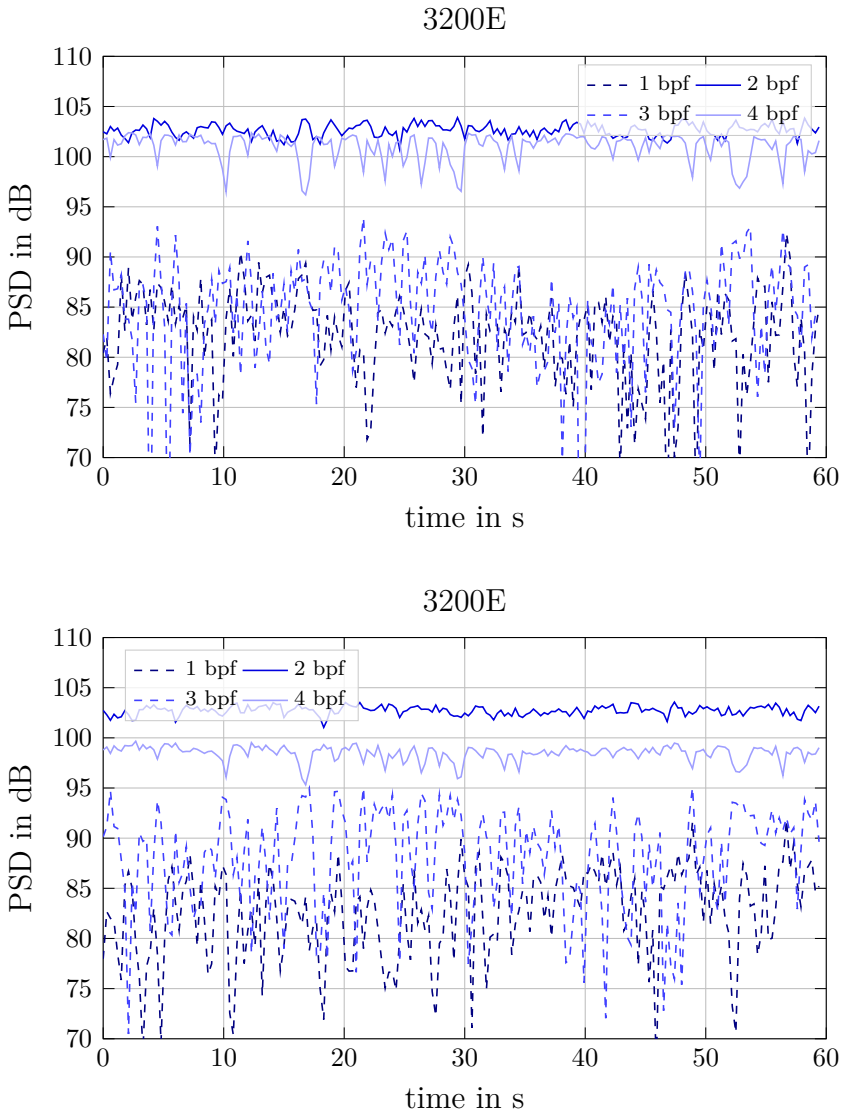

Figure 5.7: FFT components of each block of the first four BPF as power spectral density in dB resp. $^{20\,\mu Pa}/_{\sqrt{Hz}}$. Microphone closest to the rotor (top figure) resp. farthest from the rotor (bottom figure).

The figures above show the spectrogram (fig. 5.6) and the BPF components of each FFT window (fig. 5.7) of a single microphone, the microphone that is closest to the rotor in the line array is depicted in the spectrogram and in the top figure of figure 5.7. The BPF components of each FFT Window, for the microphone, that is the farthest away from the rotor in the line array is shown in the bottom figure. Note that at this operating point the rotor stator interaction mode for 3BPF (m=10) is just above its cut-on frequency of 2825 Hz with $3 \cdot \text{BPF} = 2880\,\text{Hz}$. But as the mode is propagating against the spinning direction of the rotor rotation, it is possibly blocked by the rotor blades. The rotor stator interaction mode at 4BPF ($m = -8$) is also cut-on, but a lower amplitude is measured at the microphone farther upstream, while the amplitude at 2BPF remains rather constant. This effect might be explained with phase differences between different radial orders. In that case this effect should not be present at lower rotor speeds when only one radial order is cut-on at 4BPF. In figure 5.8 the first four BPF harmonics at the operating point 2000E

are shown for the two microphones. The amplitude at 4BPF remains rather constant while the 2BPF significantly decreases in amplitude, because the rotor stator interaction mode ($m = -4$) is cut-off at this frequency.

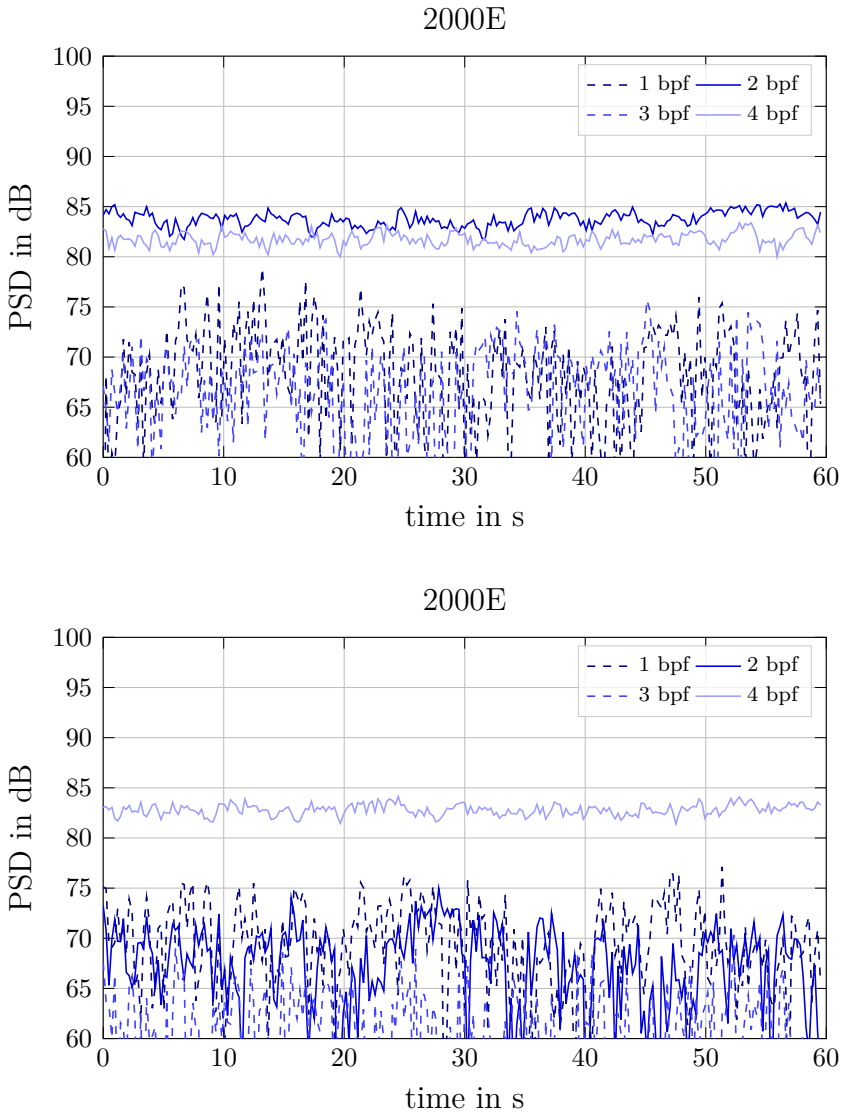

Figure 5.8: FFT components of each block of the first four BPF as power spectral density in dB resp. $^{20\,\mu Pa}/\sqrt{Hz}$. Microphone closest to the rotor (top figure) resp. farthest from the rotor (bottom figure).

5.4 Cyclostationary Analysis

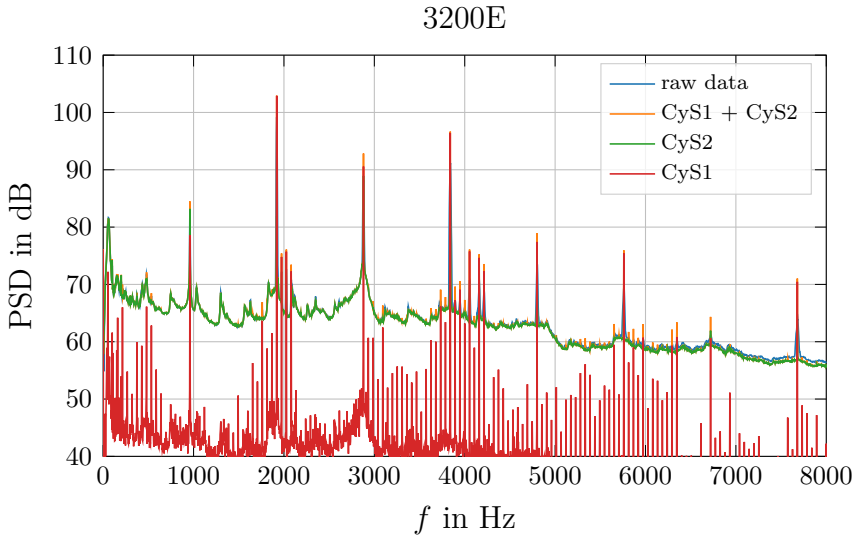

Figure 5.9: Auto power density Spectra, mean over all microphones with block length $N_b = 16384$. The spectra are normalized as power spectral densities in dB resp. $^{20\,\mu Pa}/_{\sqrt{Hz}}$.

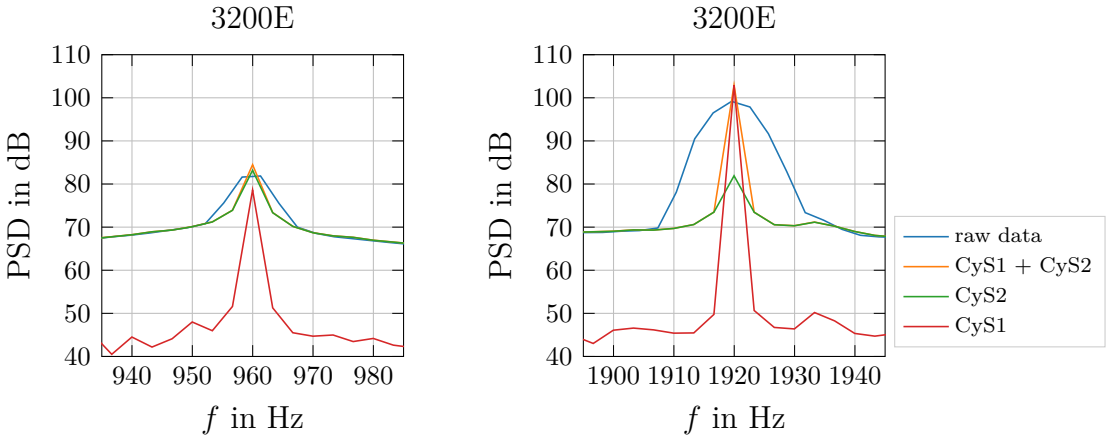

Figure 5.10: Effect of resampling and cyclo stationary analysis on cut-off BPF and cut-on 2 BPF. The spectra are normalized as power spectral densities in dB resp. $^{20\,\mu Pa}/_{\sqrt{Hz}}$.

Above 2 BPF and 4 BPF multiple pure tones are detected. It is shown below, that they have the azimuthal order $m = EO - kV$. It is supposed, that modes with the same spinning direction as the rotor are stronger due to transmission effects. Multiple pure tones have also been studied by Moreau et al. [6]:

> Under subsonic rotor speed conditions rotor-locked integral engine orders (multiple pure tones) may be excited by a strong blade flow non-uniformity, which can be generated by geometrical blade-to-blade non-uniformities or flow separation.

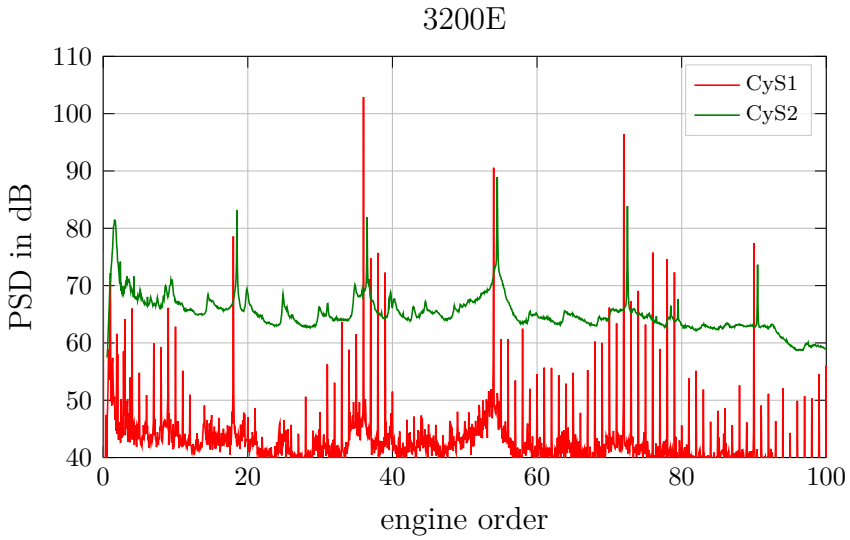

Figure 5.11: The cyclo stationary spectra CyS1 and CyS2 are normalized as power spectral densities in dB resp. $^{20\,\mu Pa}/_{\sqrt{Hz}}$.

Geometrical blade-to-blade non-uniformities are excluded, so the cause of these tones, which were also detected with the TEB rotors, is not fully explained. The turbulent flow at the outer duct wall is still non-homogenous with the used ICD Oertwig [7], which could explain the multiple pure tones. An other possible explanation includes a rotor locked amplitude modulation of the 2 bpf.

At 3 bpf the Tyler-Sofrin mode $m = 10$ has a propagation angle of angle of 35.8° and is therefore nearly parallel to the stator vane leading edge with an angle of 34° and is excited at a lower amplitude than the 2 bpf and 4 bpf. This effect is explained with dipole shaped sources on the the stator leading edge: the dipole distribution can not excite modes with a propagation angle perpendicular to the dipole axis [5].

The stator could have a higher effect on the noise than assumed. This is implied by CFD results, that show strong flow separations at the stator trailing edge. The stator is also not that perfectly assembled (weldings and vane to vane distance) which leads to irregularities in the potential field. It is to be investigated further whether this has a relevant or measurable effect.

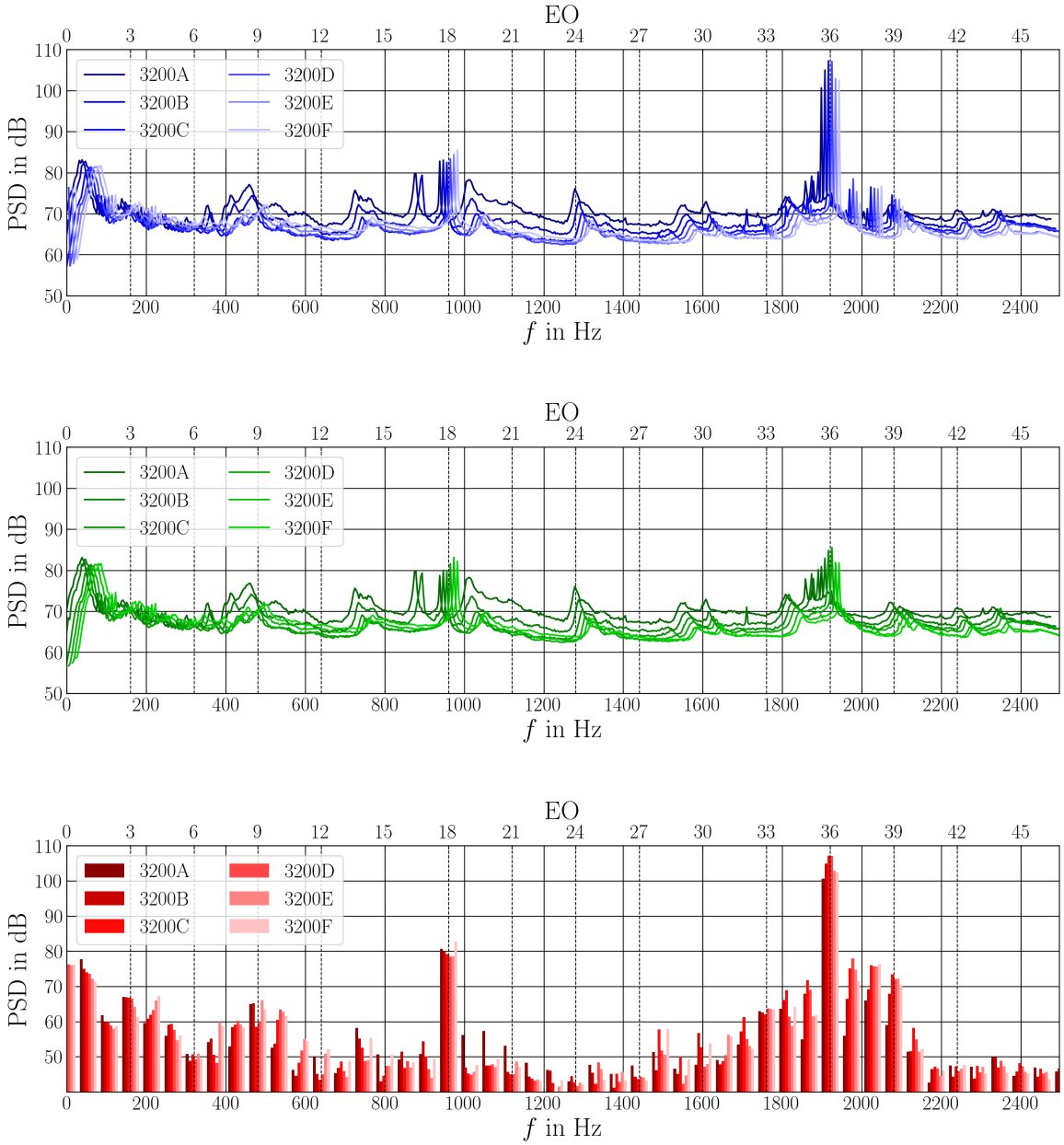

Figure 5.12: Sound pressure levels for different operating points at constant speed, mean over auto spectral densities of all microphones. The spectra are normalized as power spectral densities in dB resp. $^{20\,\mu Pa}/_{\sqrt{Hz}}$.

The narrow band components around 900 Hz may be related to noise sources that are not related to the rotor. This may be verified by comparing different operating points with different rotor speeds, but similar mass flow, for example 3200A, 3000B, 2800C and 2500E (see fig. 2.6).

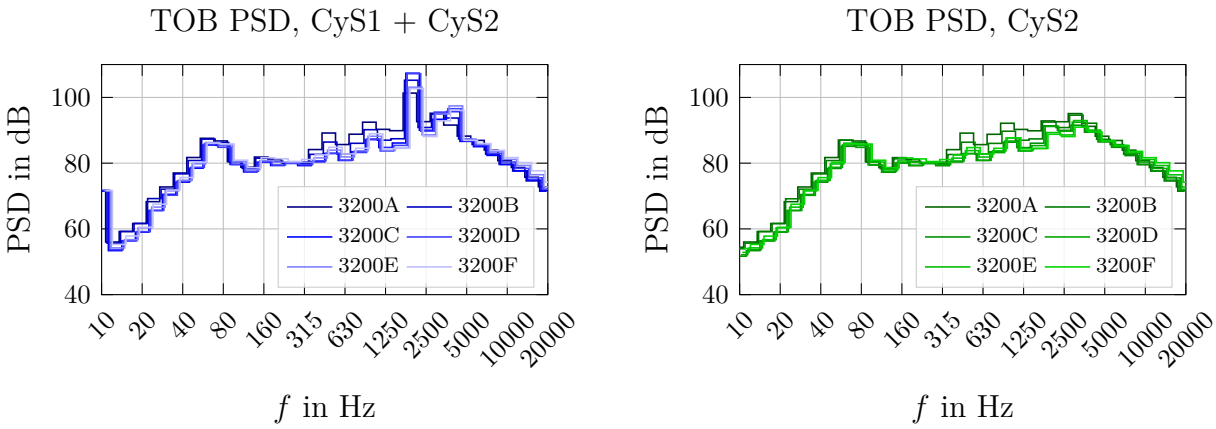

(a) resampled

(b) CyS2

Figure 5.13: Sound pressure levels as third octave band spectra for different operating points at constant speed, mean over auto spectral densities of all microphones. The spectra are normalized as power spectral densities in dB resp. $^{20\,\mu Pa}/\sqrt{Hz}$.

Test point 3200D seems to be the aerodynamic optimal operting point, as the 2 BPF is very dominant and the broadband noise seems to be the lowest. This is better visilble in the third octave band spectra. Note that the design point is 3200E. The BPF tone is cut-off, but similarly dominant as in the experiments with the previous TEB rotor [11], this seems plausible, as the same ICD was used, hence the inflow distortions should be similar.

The spectra still contain characteristics, that are presumably not caused by the rotor, but by the properties of the test rig. Comparisons with earlier Measurements with the TEB and CFK Rotors are required for a deeper understanding.

5.5 Stall Measurement

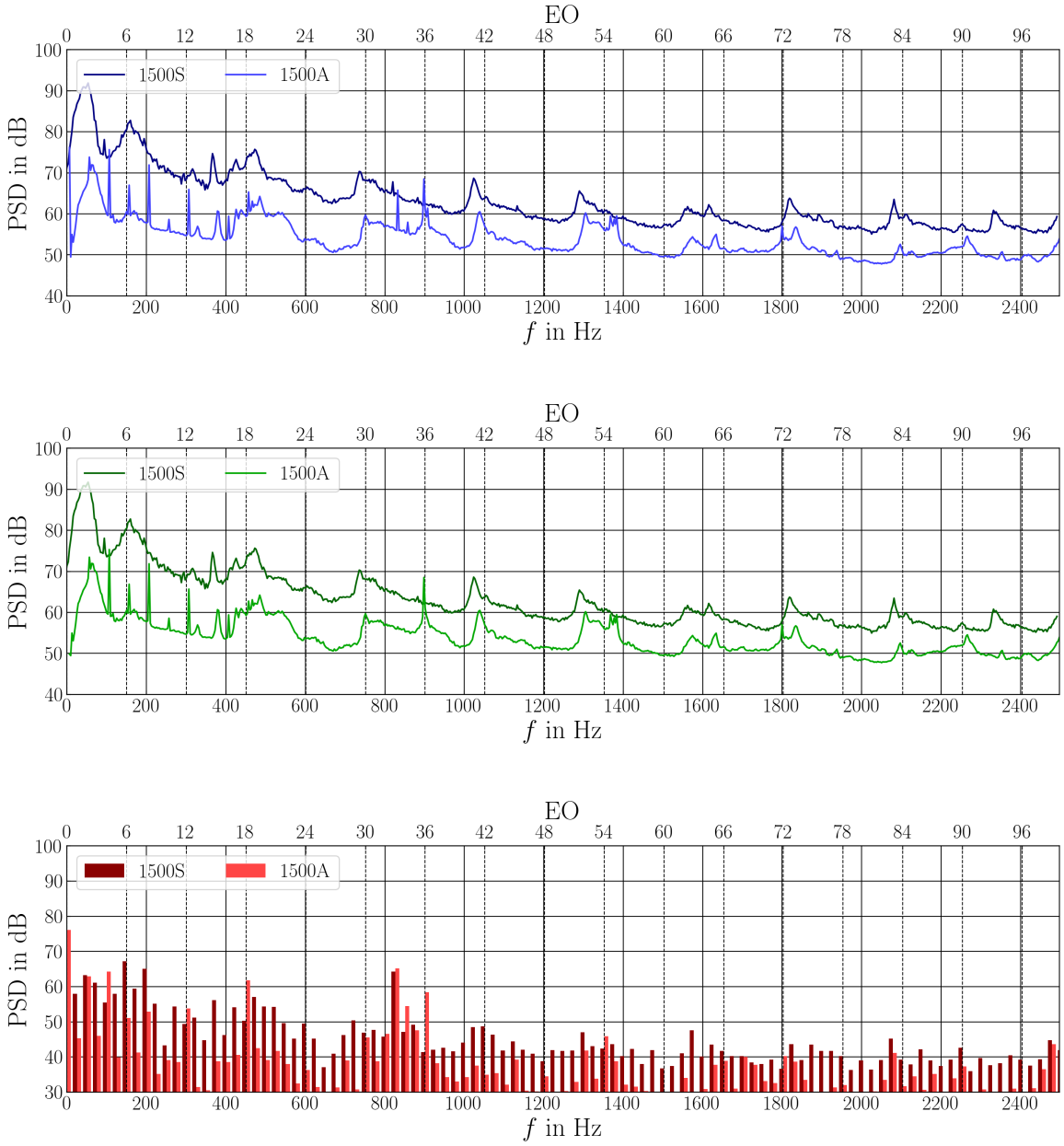

Figure 5.14: Mean over auto spectral densities of all microphones. The spectra are normalized as power spectral densities in dB resp. $^{20\,\mu Pa}/_{\sqrt{Hz}}$.

At the rotor speed of 1500 RPM an additional measurement was performed, with the throttle closed at a position where stall was detected. This operating point is labeled 1500S. In figure 5.14 this measurement is compared to the operating point 1500A. The stall results in high broadband noise, especially in the lower frequency area. The CyS1 spectrum of the operating point 1500A shows three dominant frequencies at the fist two BPFs and at the engine order 33. The operating point with stall generally shows higher amplitudes for most engine orders, but the BPF tones are not dominant. The engine

order 33 however is still dominant. This phenomenon is not understood and could be investigated further in future analysis. Open questions related to this are:

- How big is the gap between rotor tip and casing?
- Is the engine order 33 a sum difference tone (*Summendifferenzenton*)? If it is, why aren't there two symmetric tones around the engine order 36?
- Is there an analytic formula for the stall rotation speed?
- Is the measurement time of 20 s too short? A SNR evaluation for this measurement might give some insight.
- A possible analysis tool for a further investigation is the cyclostationary analysis with the Wigner-Ville spectrum. And the short time AMA and RMA.

6 Mode Analysis Results

In this section the results of the AMA, RMA and short time AMA and RMA are shown.

6.1 AMA

The AMA results shown here are calculated with Ring6: The ring array closest to the rotor with 36 microphone positions.

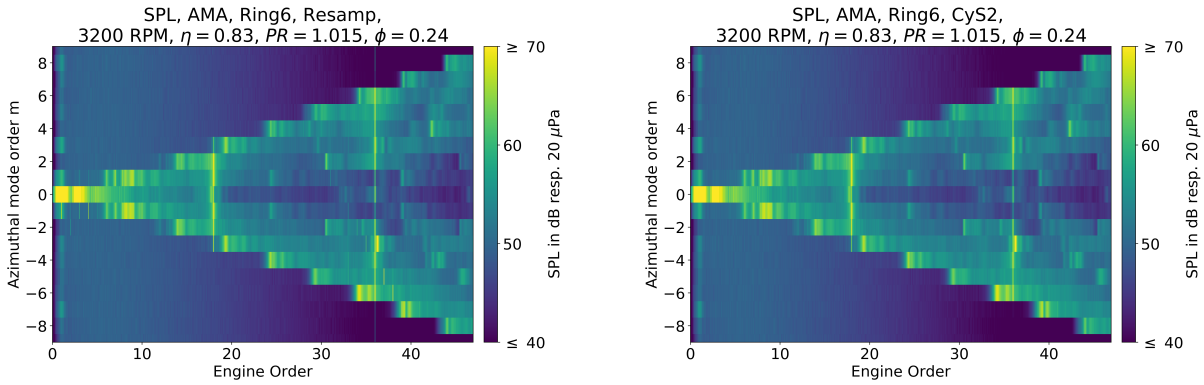

Figure 6.1: Narrow band AMA at operating point 3200E, the total spectrum (Cys1+Cys2) on the left and Cys2 spectrum on the right.

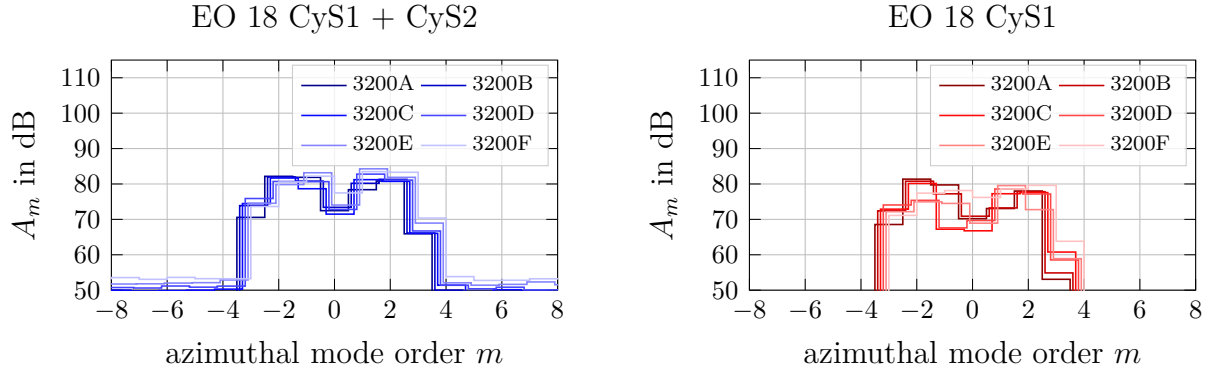

Figure 6.2: Modal Amplitudes as SPL in dB resp. 20 µPa.

The modal spectrum is quite flat and symmetrical. Further understanding is provided by the short time AMA in section 6.3.

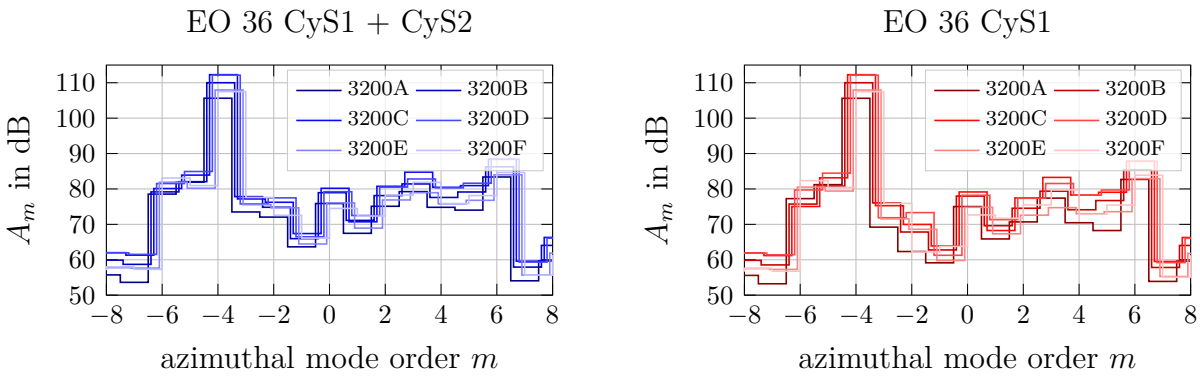

Figure 6.3: Modal Amplitudes as SPL in dB resp. 20 µPa.

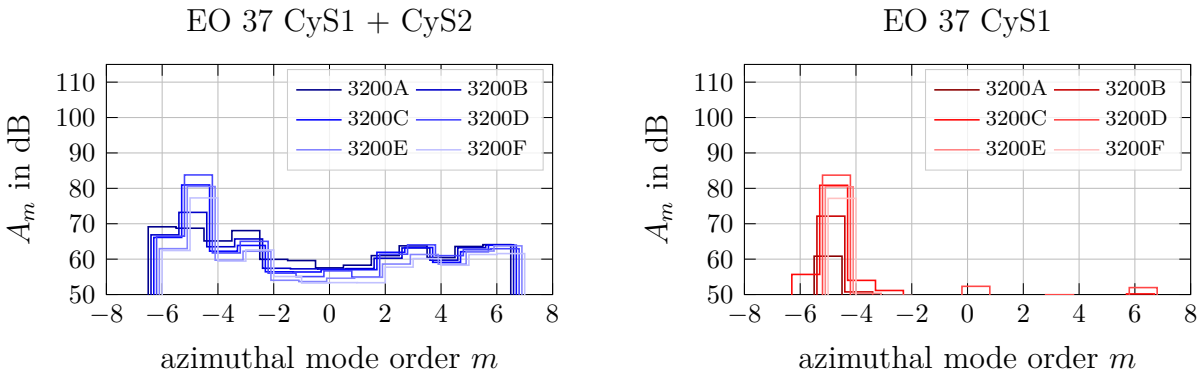

Figure 6.4: Modal Amplitudes as SPL in dB resp. 20 µPa.

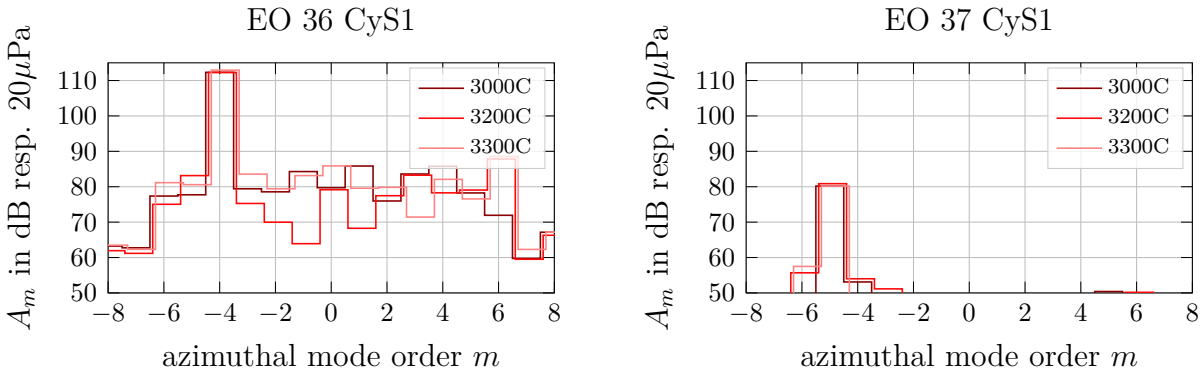

Figure 6.5: Modal Amplitudes as SPL in dB resp. 20 µPa.

6.2 RMA

6.2.1 Tonal

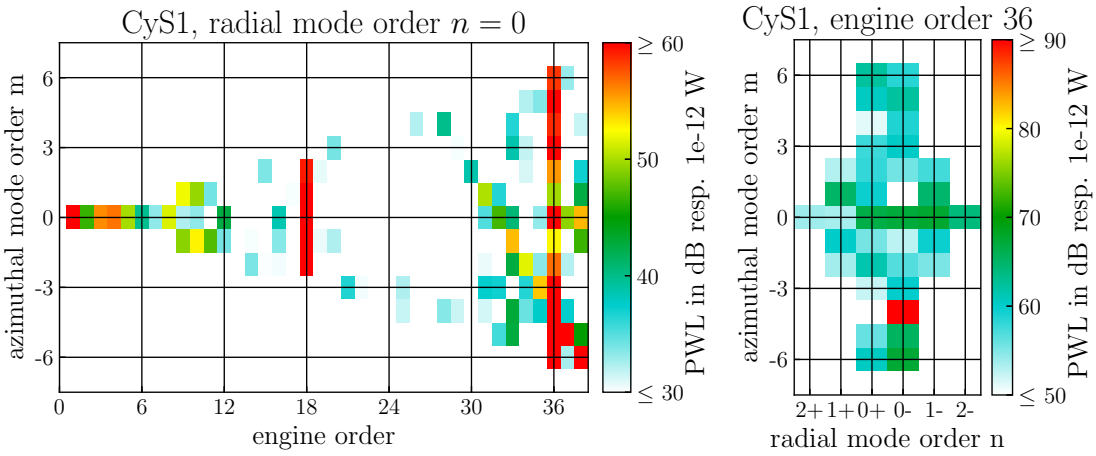

Figure 6.6: Modal decomposition of the sound field at test point 3200E.

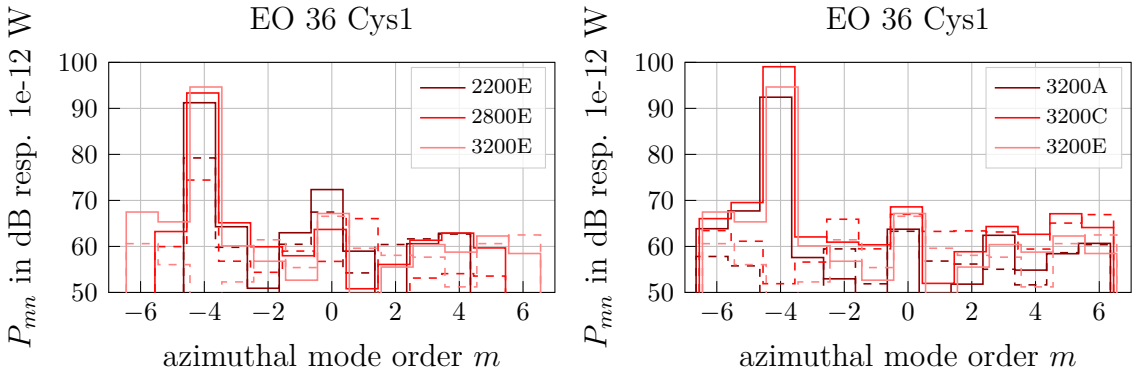

Figure 6.7: Comparison of sound power levels of 2 BPF for different operating points.

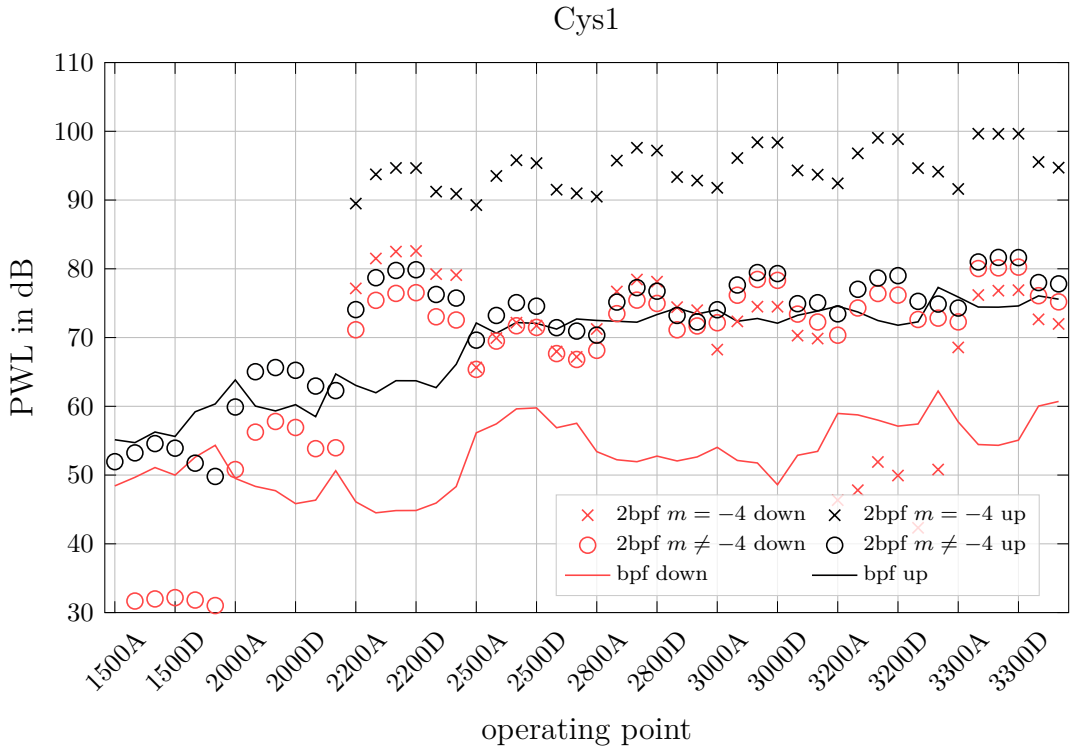

Figure 6.8: Modal sound power level (PWL) in dB resp. 10^{-12}W. The labels for the operating points that end with B, C, E and F are not shown to increase readability. The Tyler-Sofrin mode $m = -4$ at 2 BPF is denoted with x marks and is still cut-off at 2000 RPM. The dots mark the sum over all modal sound power amplitudes up- resp. downstream at 2 BPF except for the Tyler-Sofrin mode. The solid lines mark the sum over all modal sound power amplitudes up- resp. downstream at BPF. The sound power of the upstream propagating modes is increasing with higher rotor speed. At 2 BPF a repeating pattern is noticed. This pattern can be explained with the flow coefficient, see also figure 6.9. Interestingly, at BPF no such pattern can be found.

Different flow conditions at constant rotor speed lead to different shapes of the rotor wakes. Therefore the acoustic energy of the rotor stator interaction is distributed differently between the harmonics of the BPF.

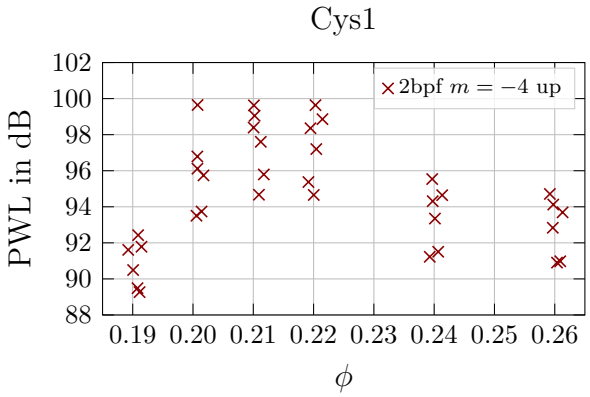

Figure 6.9: As shown in equation (2.1), the flow coefficient ϕ is defined as the ratio of the inlet and rotor tip speeds. Therefore it scales with the incidence angle at the leading edge of the rotor. At low mach numbers it is plausible to assume, that this also leads to similar incidence angles of the rotor wakes on the vanes. One can conclude, that the source strength of the Tyler-Sofrin mode at constant incidence angle increases up to 6 dB, when the mach number is raised by 50 % (from 2200 RPM to 3300 RPM).

6.2.2 Broadband

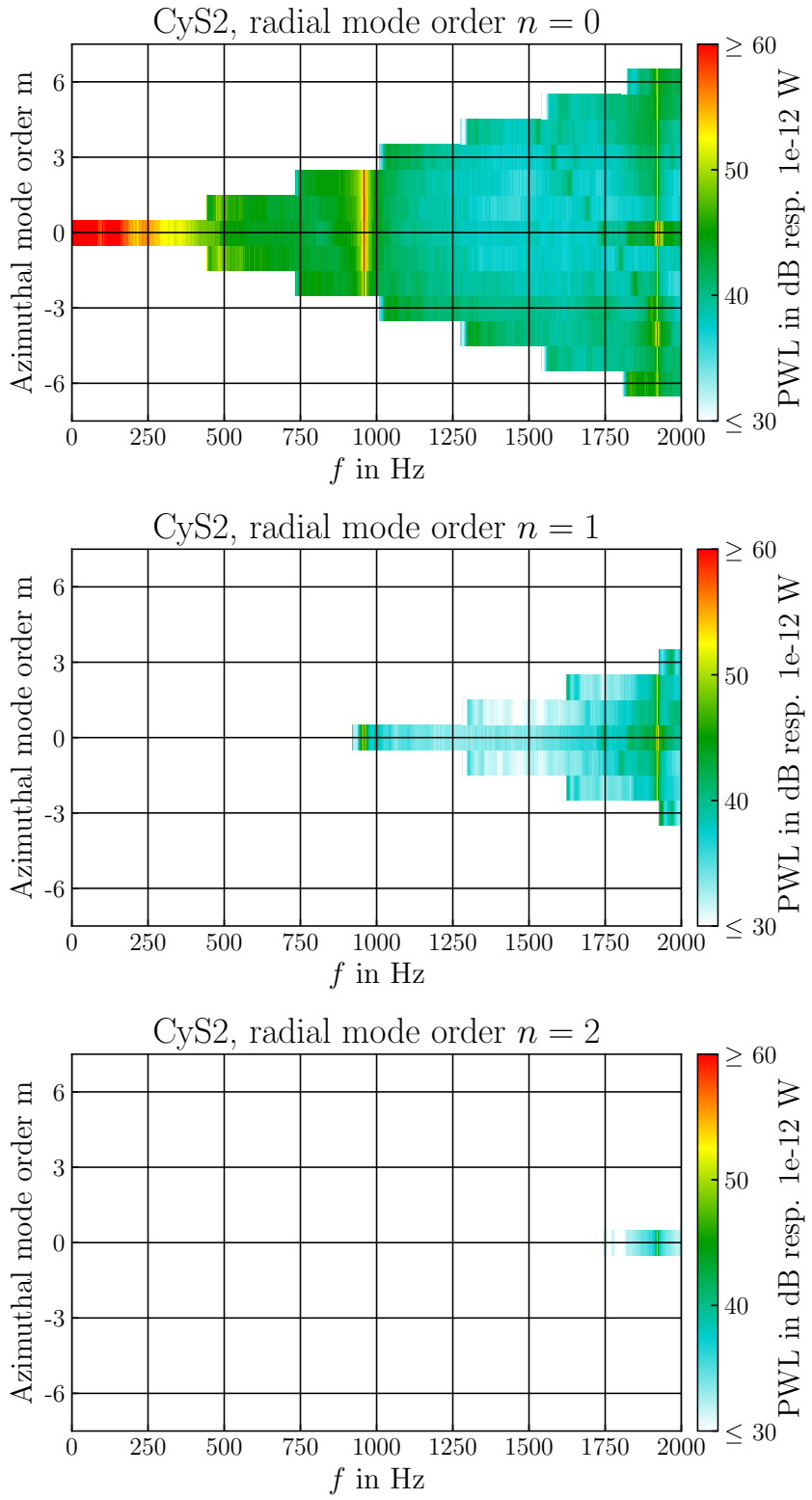

Figure 6.10: Upstream propagating modes at the design point 3200E. An intensive comparison in the domain of radial modes with the results presented in [11] remains open.

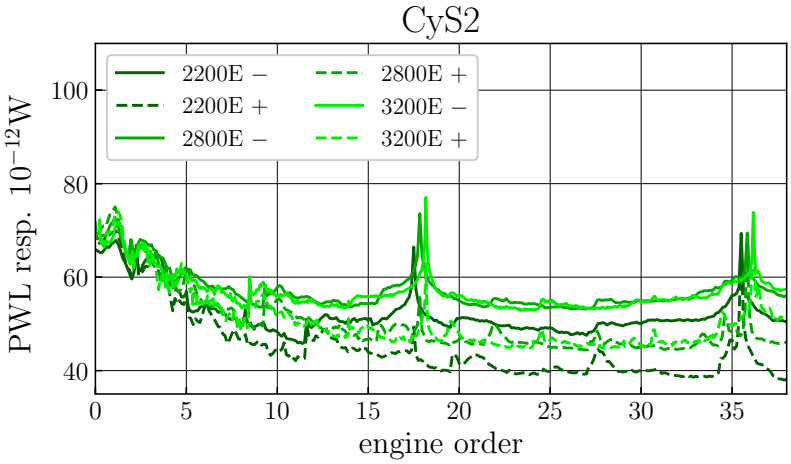

(a) $\Phi = \text{const.}$

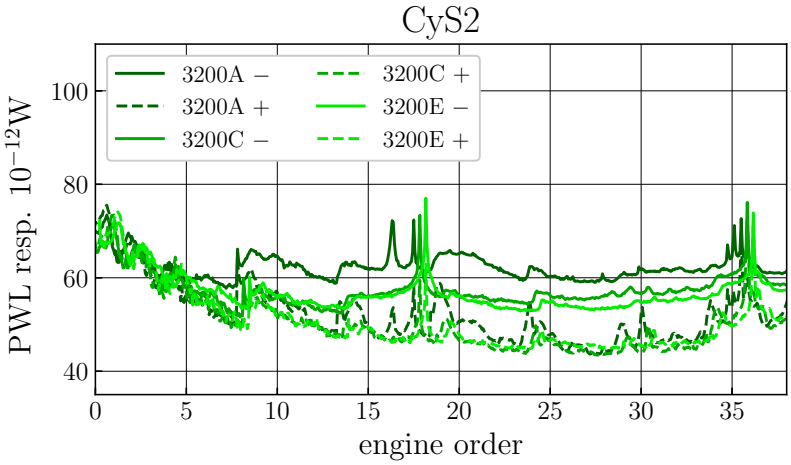

(b) $U_{\text{tip}} = \text{const.}$

Figure 6.11: Comparison of broadband sound power spectra at different operating points at constant flow rate or rotor speed.

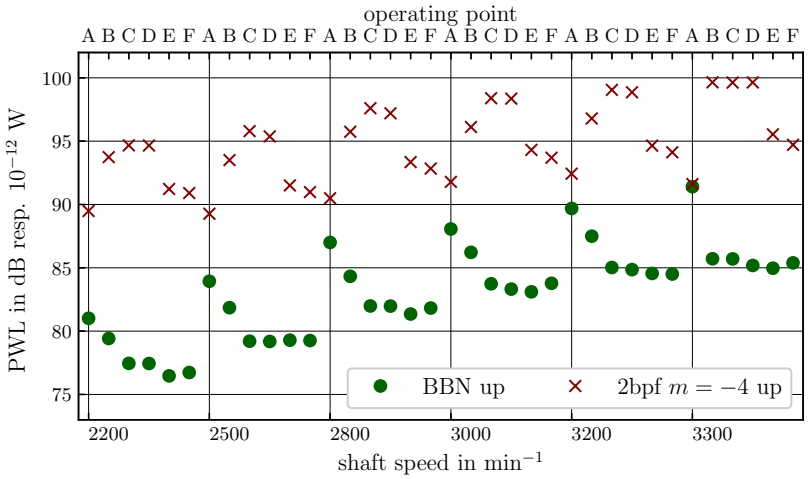

Figure 6.12: Integrated broadband sound power level and comparison with Tyler-Sofrin mode. The broadband noise increases with approximately the fifth power of rotor speed. For the varying flow rate a repetitive pattern is found: High broadband noise values at the two lowest flow rates and a plateau at medium and high flow rates.

6.3 Short Time Mode Analysis

In this section the results for the short time RMA at the first two BPF harmonics, and the results of a short time AMA at the first four BPF harmonics are shown. Analysis of the multiple pure tones (engine orders 37 and 38) are possible further investigations.

Oertwig [7] also investigated the behaviour of the phase in a short time analysis. This is not done here, but would be an interesting investigation.

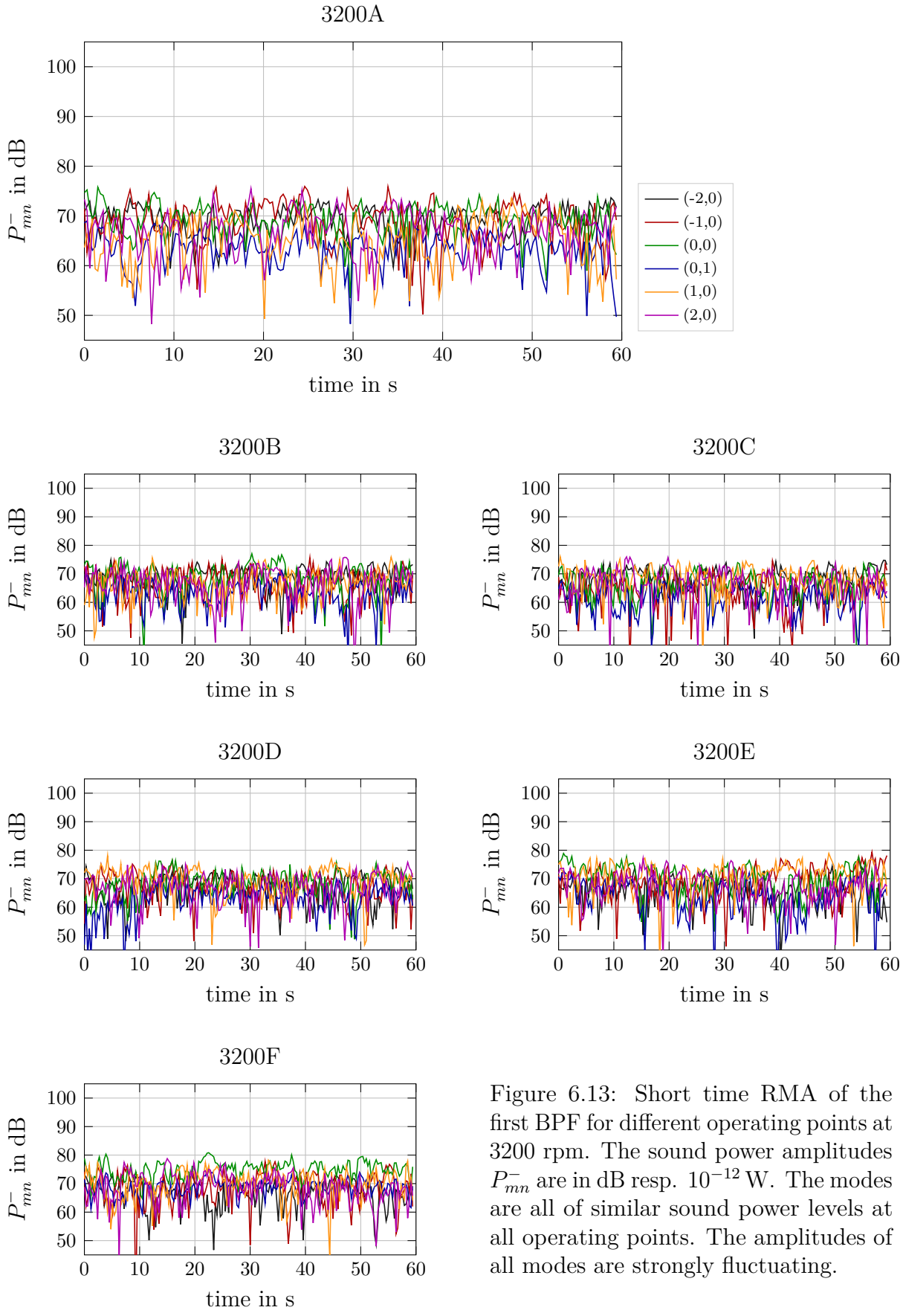

Figure 6.13: Short time RMA of the first BPF for different operating points at 3200 rpm. The sound power amplitudes P_{mn}^- are in dB resp. 10^{-12} W. The modes are all of similar sound power levels at all operating points. The amplitudes of all modes are strongly fluctuating.

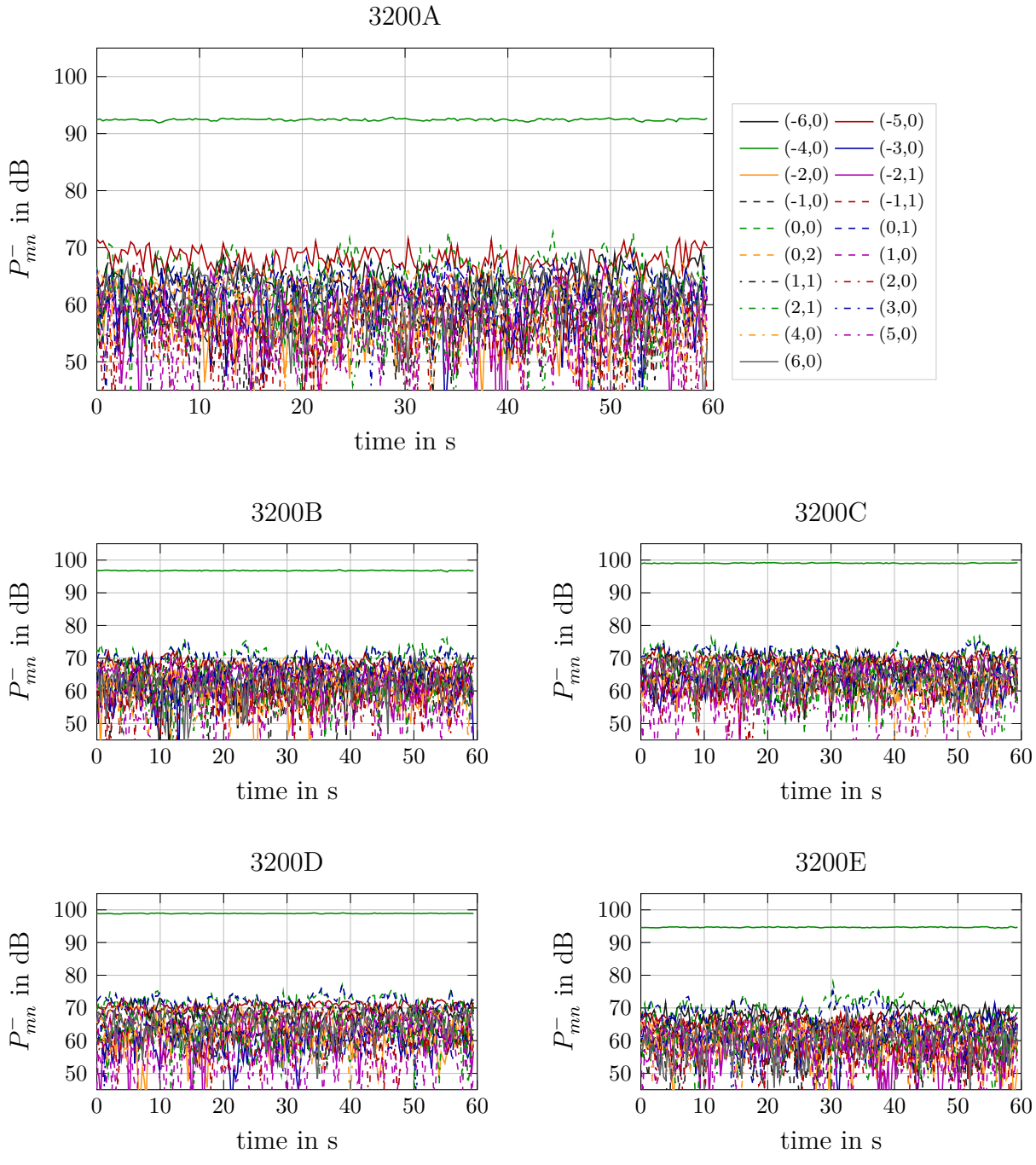

Figure 6.14: Short time RMA of the second BPF for different operating points at 3200 rpm. The sound power amplitudes P_{mn}^- are in dB resp. 10^{-12} W. The Tyler Sofrin mode is excited with very constant amplitude at all operating points with at least 20 dB distance to the other mode orders. The other modes are all with strongly fluctuating amplitudes.

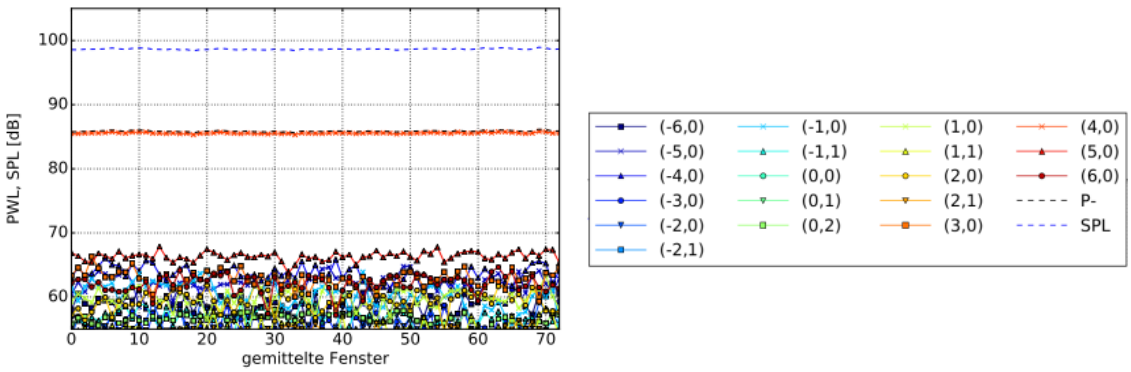

Figure 6.15: Figure 5.23(e) from Oertwig [7]: Short time RMA at 2 BPF at 3000 RPM, averaged over 10 FFT-windows. Although a different Rotor was used by Oertwig, the results are rather similar.

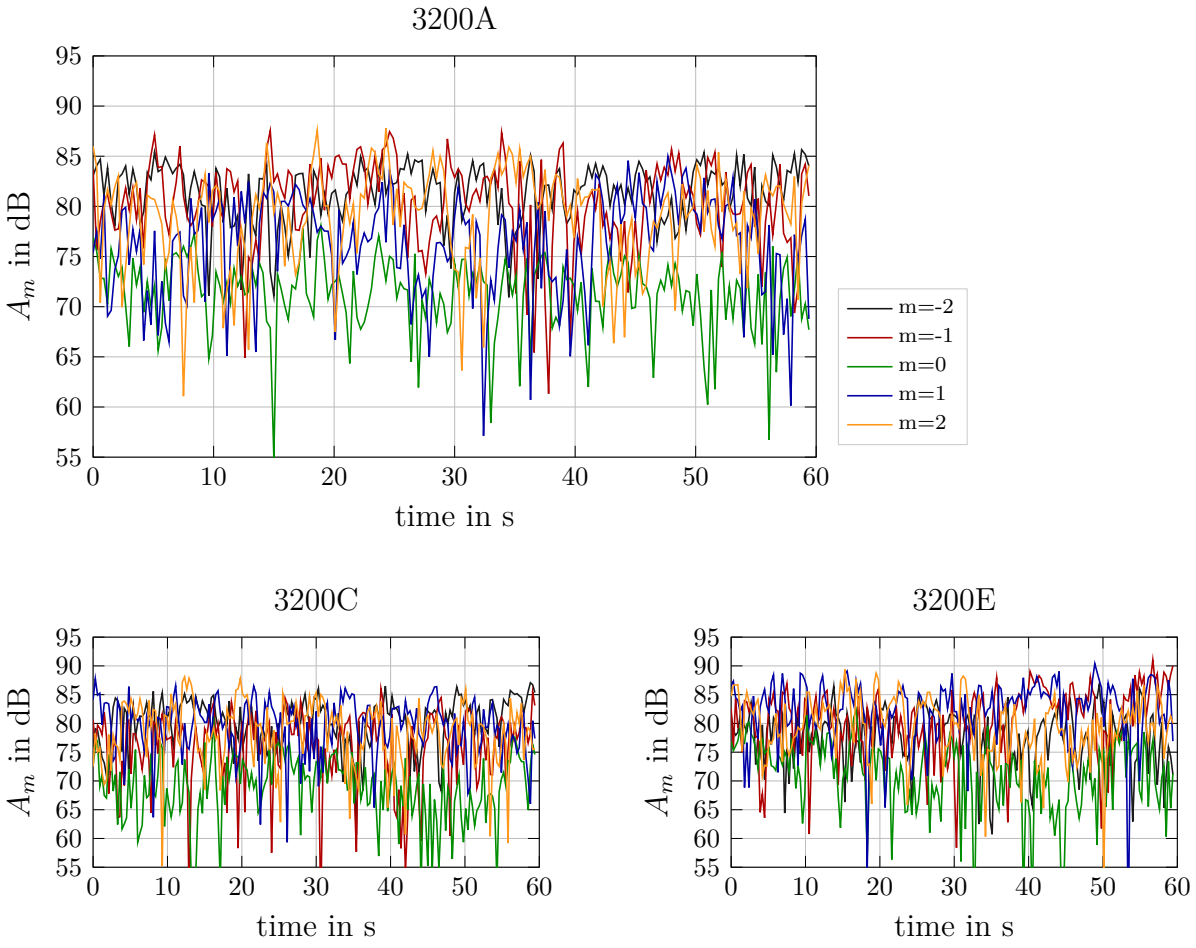

Figure 6.16: AMA for each FFT window at the first BPF. The azimuthal mode amplitudes are in dB resp. 20 µPa.

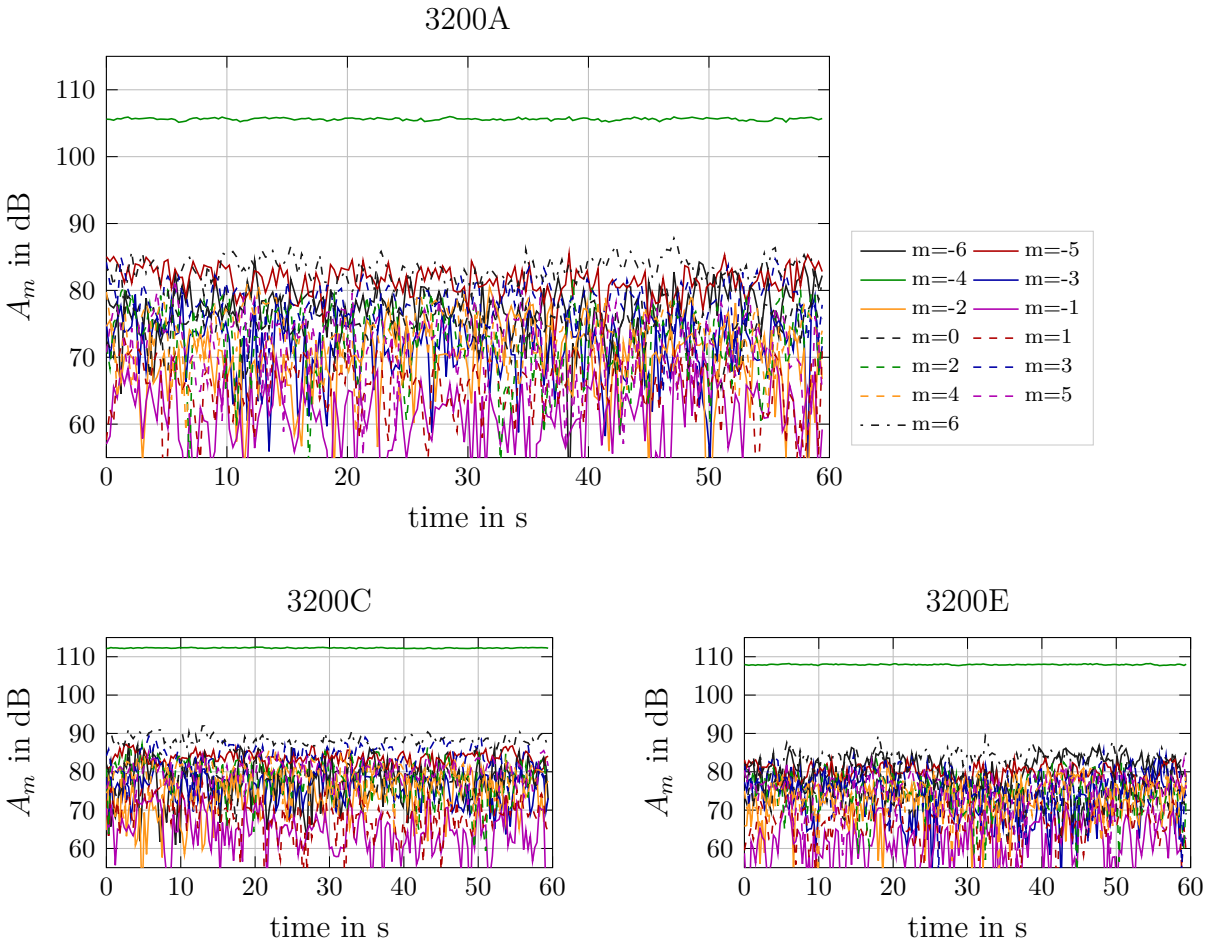

Figure 6.17: AMA for each FFT window at 2 BPF. The azimuthal mode amplitudes are in dB resp. 20 µPa.

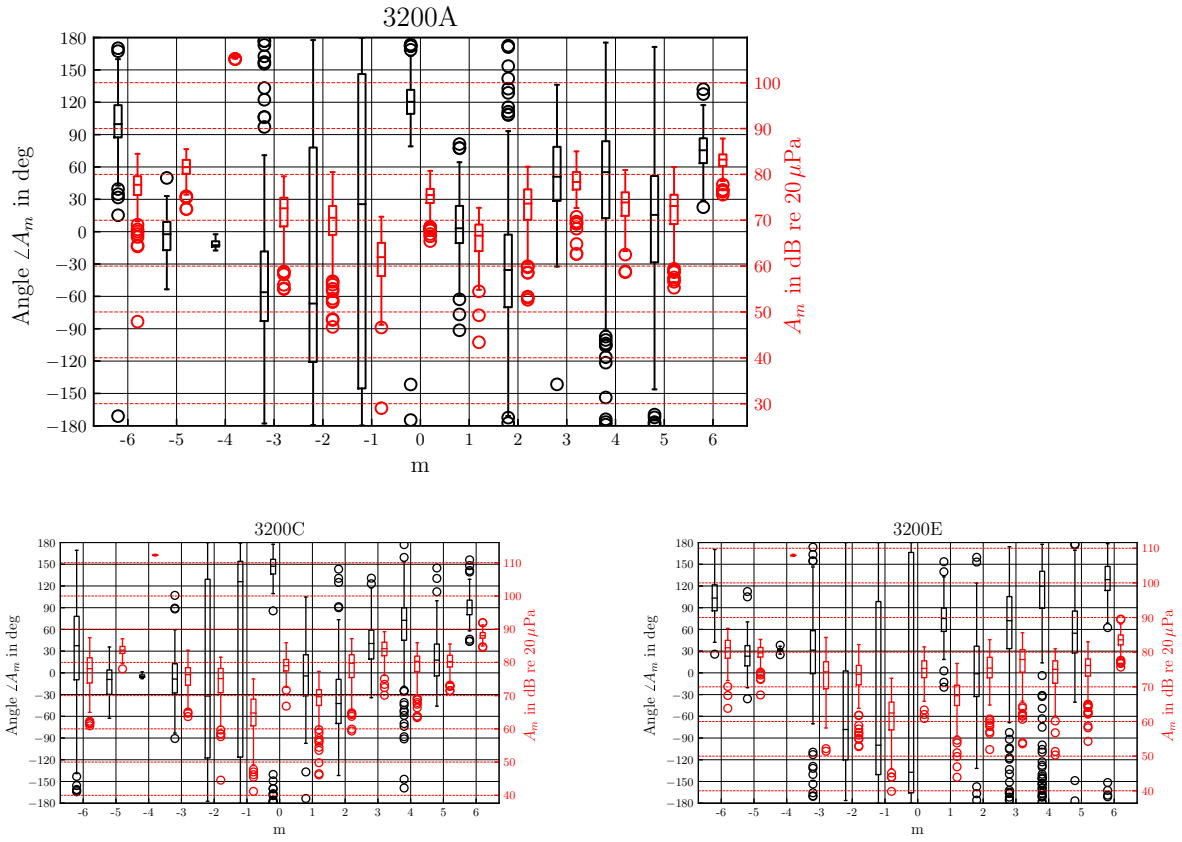

Figure 6.18: Mode angles of short time AMA for each FFT window at 2 BPF.

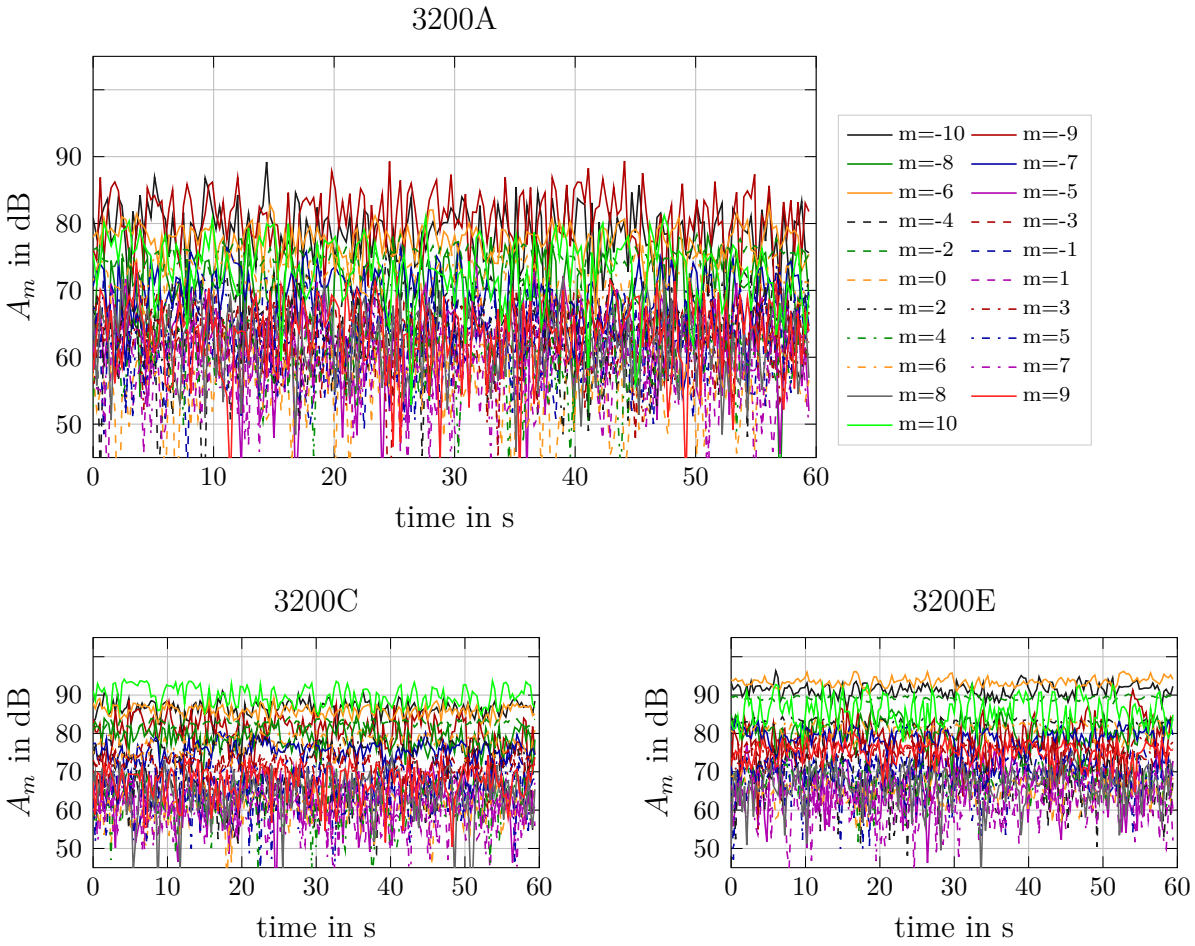

Figure 6.19: AMA for each FFT window at 3 BPF. The azimuthal mode amplitudes are in dB resp. 20 µPa.

Guérin et al. [5] showed with a dipole distribution on the stator leading edge, that modes with a propagation angle perpendicular to the dipole axis are not excited. Here the Angle at the leading edge of the stator is 34° while the propagation angle of the Tyler-Sofrin mode at 3 BPF is 36°, for the test point 3200E.

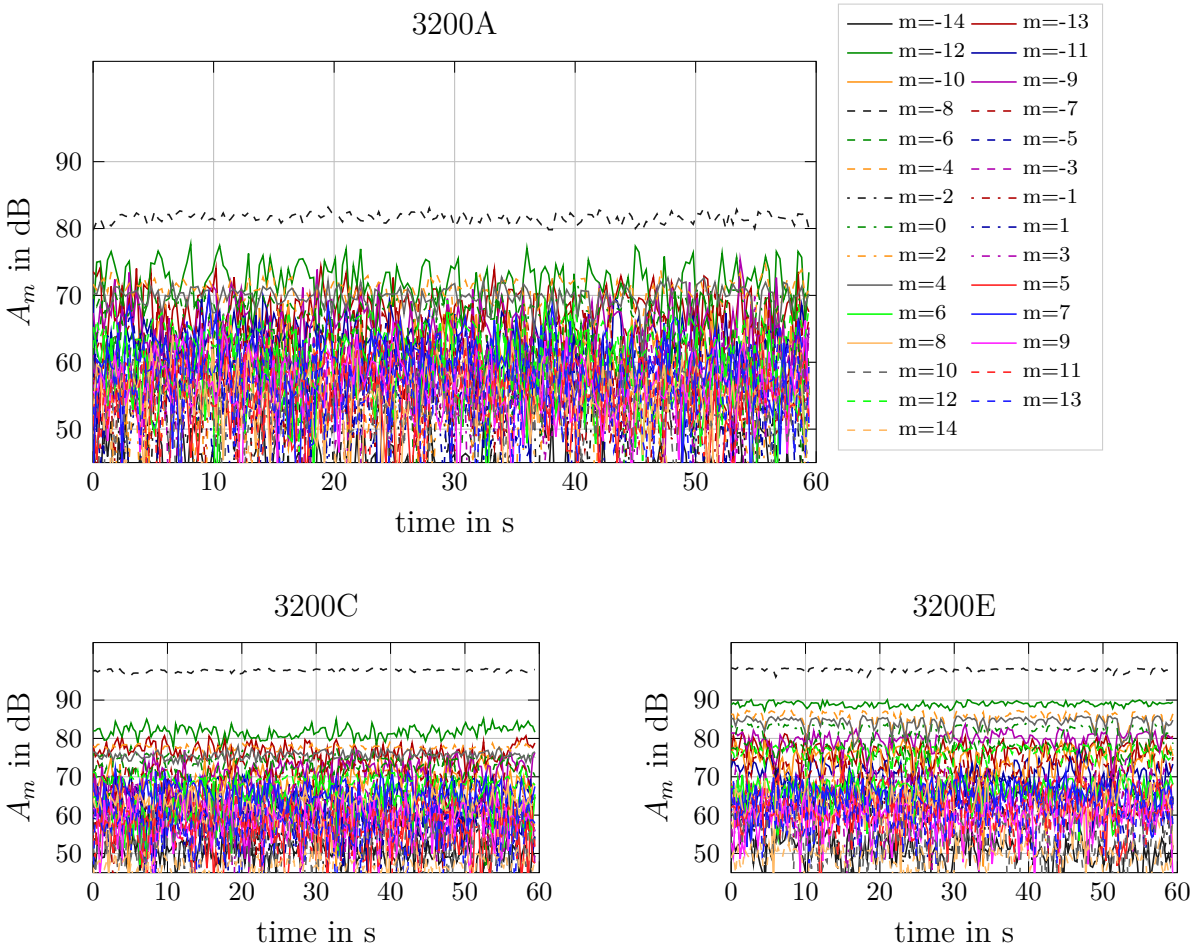

Figure 6.20: AMA for each FFT window at 4 BPF. The azimuthal mode amplitudes are in dB resp. 20 µPa.

The Question occurred whether the atypical pure tones at the engine orders 37,38 arise from a strong fluctuating amplitude and would therefore be reduced by a longer measurement time. The Results of a short time AMA at engine order 37 show, that these tones are distinct rotor locked tones. The results at two different flow coefficients are shown in figures 6.21 - 6.23

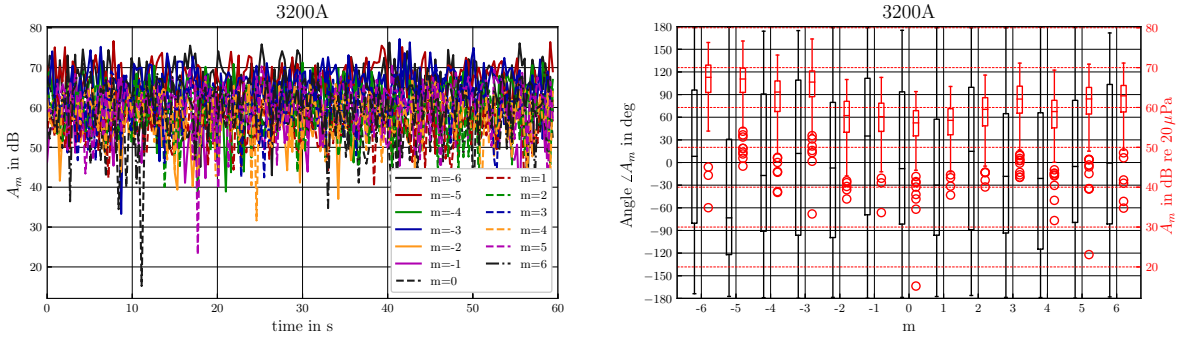

Figure 6.21: Short time AMA for each FFT window at engine order 37 (left) and box-plot of the mode angles (right) at operating point 3200A. The azimuthal mode amplitudes are in dB re 20 µPa.

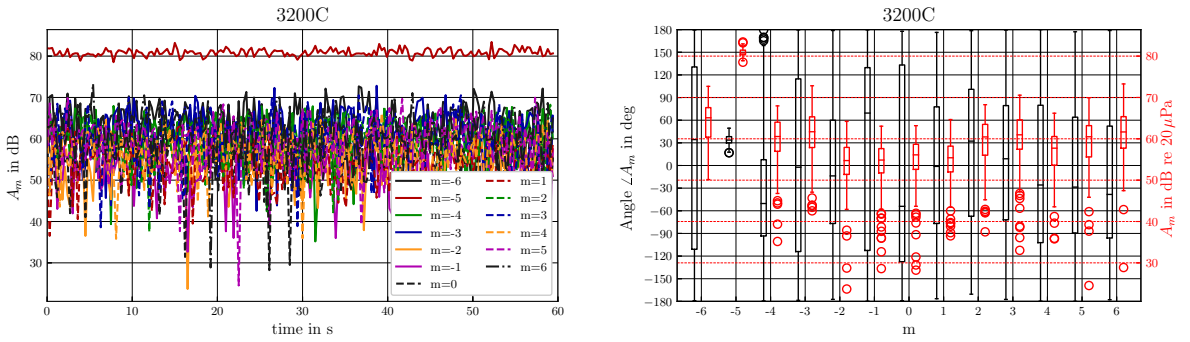

Figure 6.22: Short time AMA for each FFT window at engine order 37 (left) and box-plot of the mode angles (right) at operating point 3200C. The azimuthal mode amplitudes are in dB re 20 µPa.

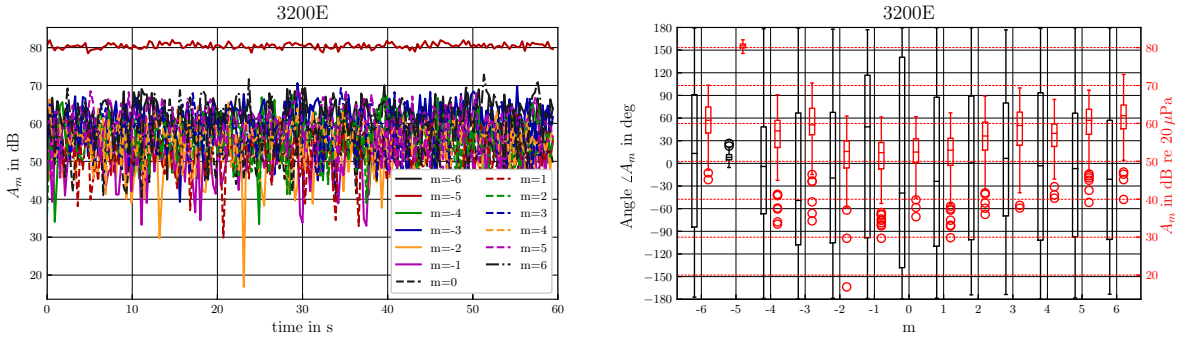

Figure 6.23: Short time AMA for each FFT window at engine order 37 (left) and box-plot of the mode angles (right) at operating point 3200E. The azimuthal mode amplitudes are in dB re 20 µPa.

6.4 Possible further Analyses

As the array contains an axial array, the wave number decomposition technique or the CAAS method could be applied. This measurement data could also be used for the EAMA method. An extended azimuthal mode analysis with two microphone rings. With this method advanced sound power estimation methods can be tested.

A Appendix

Table A.1: Test matrix with aerodynamic parameters, measured 11.10.2018.

Label	RPM	M_{tip}	M_{inlet}	Π	T_{amb}	η	ϕ	ψ
1000A	1000.5	0.069	0.013	1.0016	292.27	0.56	0.19	0.49
1000B	1000.95	0.069	0.014	1.0016	292.42	0.59	0.2	0.48
1000C	999.45	0.069	0.015	1.0016	292.31	0.58	0.21	0.48
1000D	1000.8	0.069	0.015	1.0015	292.42	0.58	0.22	0.45
1000E	999.45	0.069	0.017	1.0013	292.1	0.57	0.24	0.4
1000F	1000.35	0.069	0.018	1.0011	292.16	0.54	0.26	0.34
2000A	2001.6	0.139	0.026	1.0068	291.49	0.74	0.19	0.5
2000B	2002.8	0.139	0.028	1.0067	291.42	0.76	0.2	0.5
2000C	1998.75	0.139	0.029	1.0066	291.39	0.78	0.21	0.49
2000D	2000.25	0.139	0.03	1.0063	291.43	0.78	0.22	0.47
2000E	1997.1	0.139	0.033	1.0057	291.44	0.76	0.24	0.43
2000F	1999.35	0.139	0.036	1.005	291.4	0.74	0.26	0.37
2500A	2499.6	0.173	0.033	1.0106	291.41	0.77	0.19	0.51
2500B	2500.05	0.174	0.035	1.0106	291.4	0.78	0.2	0.5
2500C	2500.35	0.174	0.037	1.0103	291.35	0.79	0.21	0.49
2500D	2500.5	0.174	0.038	1.01	291.25	0.81	0.22	0.48
2500E	2501.85	0.174	0.042	1.009	291.28	0.8	0.24	0.43
2500F	2505.15	0.174	0.045	1.0078	291.27	0.77	0.26	0.37
3000A	2997.9	0.208	0.04	1.0154	291.83	0.76	0.19	0.51
3000B	3002.55	0.208	0.042	1.0153	291.77	0.82	0.2	0.51
3000C	3003.0	0.208	0.043	1.015	291.72	0.81	0.21	0.5
3000D	3001.8	0.208	0.045	1.0146	291.77	0.84	0.22	0.48
3000E	2997.3	0.208	0.05	1.0132	291.69	0.8	0.24	0.44
3000F	3000.75	0.208	0.054	1.0113	291.55	0.81	0.26	0.37
3200A	3200.85	0.222	0.042	1.0176	292.2	0.82	0.19	0.51
3200B	3200.1	0.222	0.044	1.0175	292.12	0.83	0.2	0.51
3200C	3200.85	0.222	0.046	1.0172	292.11	0.81	0.21	0.5
3200D	3197.55	0.222	0.049	1.0165	292.07	0.83	0.22	0.48
3200E	3198.45	0.222	0.053	1.0149	291.97	0.83	0.24	0.43
3200F	3198.45	0.222	0.057	1.013	291.92	0.78	0.26	0.38

Table A.2: Test matrix with aerodynamic parameters, measured 15.10.2018.

Label	RPM	M_{tip}	M_{inlet}	Π	T_{amb}	η	ϕ	ψ
1500A	1499.4	0.104	0.02	1.0038	291.21	0.66	0.19	0.5
1500B	1499.55	0.104	0.021	1.0037	291.07	0.69	0.2	0.49
1500C	1499.4	0.104	0.022	1.0037	291.13	0.71	0.21	0.49
1500D	1500.3	0.104	0.023	1.0035	290.93	0.7	0.22	0.46
1500E	1499.55	0.104	0.025	1.0031	291.02	0.68	0.24	0.42
1500F	1499.55	0.104	0.027	1.0027	291.08	0.67	0.26	0.36
2200A	2200.35	0.153	0.029	1.0082	292.16	0.74	0.19	0.5
2200B	2200.5	0.153	0.031	1.0081	292.16	0.77	0.2	0.5
2200C	2199.45	0.152	0.032	1.008	292.07	0.79	0.21	0.49
2200D	2199.3	0.152	0.033	1.0077	292.08	0.81	0.22	0.48
2200E	2203.5	0.153	0.036	1.007	292.13	0.76	0.24	0.43
2200F	2203.2	0.153	0.04	1.006	292.2	0.75	0.26	0.37
2800A	2797.5	0.194	0.037	1.0134	290.99	0.81	0.19	0.51
2800B	2799.45	0.194	0.039	1.0133	290.85	0.83	0.2	0.5
2800C	2801.1	0.195	0.041	1.0131	290.82	0.81	0.21	0.5
2800D	2799.75	0.195	0.043	1.0126	290.72	0.82	0.22	0.48
2800E	2801.1	0.195	0.046	1.0114	290.62	0.82	0.24	0.43
2800F	2798.55	0.194	0.05	1.01	290.59	0.77	0.26	0.38
3000G	2999.25	0.208	0.04	1.0154	291.68	0.78	0.19	0.51
3000H	2999.55	0.208	0.042	1.0153	291.69	0.82	0.2	0.51
3000I	3000.15	0.208	0.043	1.0151	291.59	0.82	0.21	0.5
3000J	2997.45	0.208	0.045	1.0146	291.51	0.83	0.22	0.48
3000K	3002.55	0.208	0.05	1.0132	291.51	0.82	0.24	0.44
3000L	3003.15	0.208	0.054	1.0114	291.56	0.79	0.26	0.38
3300A	3298.2	0.229	0.043	1.0188	291.55	0.78	0.19	0.51
3300B	3302.1	0.229	0.046	1.0186	291.52	0.83	0.2	0.51
3300C	3306.0	0.229	0.048	1.0183	291.55	0.81	0.21	0.5
3300D	3298.65	0.229	0.05	1.0177	291.42	0.82	0.22	0.48
3300E	3301.2	0.229	0.055	1.016	291.2	0.84	0.24	0.44
3300F	3302.4	0.229	0.059	1.014	291.05	0.79	0.26	0.38

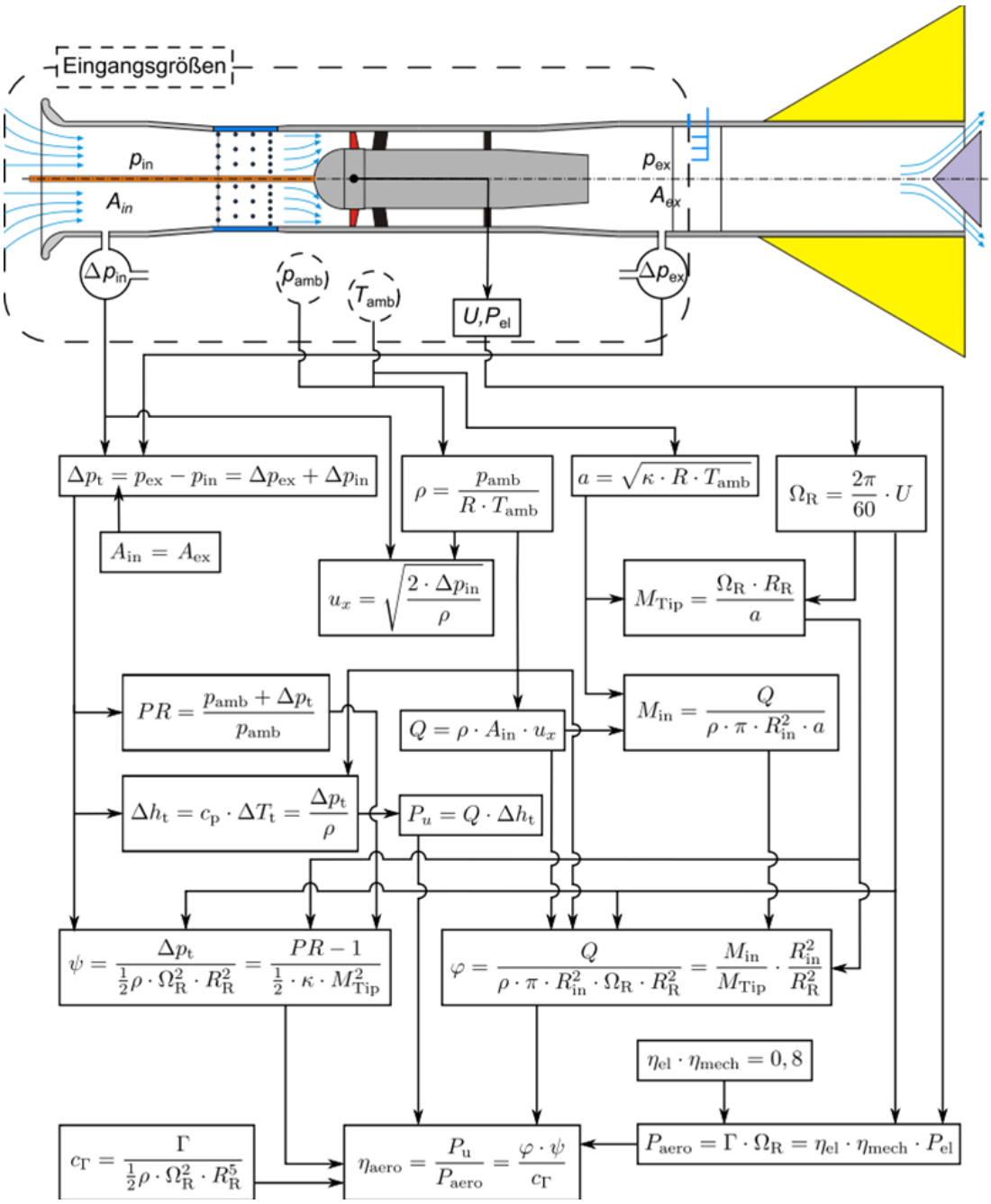

Figure A.1: Flow chart of the calculation of aerodynamic parameters from the measurement.

References

[1] *AFT FLOCON - 1 Bestimmung der aerodynamischen Kennwerte*. 1st ed. AT-TRA-AA-0004. DLR. Berlin, 2017.

[2] *AFT FLOCON - 1 Pruefstand Bedienungsanleitung*. 1st ed. AT-TRA-AA-0002. DLR. Berlin, 2017.

[3] M. Behn, B. Pardowitz, and U. Tapken. "Compressed Sensing Based Radial Mode Analysis of the Broadband Sound Field in a Low-Speed Fan Test Rig". In: *7th Berlin Beamforming Conference*. Berlin, Germany, 2018.

[4] L. C. Caldas, S. Oertwig, A. Rudolphi, R. Meyer, L. Enghardt, and U. Tapken. "Development and assessment of an inflow control device and a bell-mouth for a low-speed aeroacoustic fan rig". In: *25th AIAA/CEAS Aeroacoustics Conference*. Delft, The Netherlands, Apr. 2019, AIAA 2019–2713.

[5] S. Guérin, A. Moreau, and U. Tapken. "Relation between source models and acoustic duct modes". In: *15th AIAA/CEAS Aeroacoustics Conference*. Miami, Florida, May 2009, AIAA 2009–3364.

[6] A. Moreau, L. Enghardt, and H. Boden. "On the Relation between Broadband Noise and Fan Aerodynamic Performance". In: *Fan Noise 2007 - 3rd International Symposium on Fan Noise*. Lyon, France, Sept. 2007.

[7] S. Oertwig. "Optimierung der Einlaufströmung an einem Axialventilator-Versuchsstand und deren Einfluss auf die Akustik". Master Thesis. Berlin: Technische Universität Berlin, Apr. 2016.

[8] A. Pereira, J. Antoni, and Q. Leclère. "Empirical Bayesian regularization of the inverse acoustic problem". In: *Applied Acoustics* 97 (2015), pp. 11 –29.

[9] M. Spitalny, U. Tapken, M. Behn, and T. Gensch. *Bericht SiValT AP 1.4 Messgenauigkeit Akustik*. Interner Bericht IB-92517-1/-BXX. Deutsches Zentrum für Luft- und Raumfahrt e.V., Institut für Antriebstechnik, Abteilung Triebwerksakustik, Berlin, 2020.

[10] U. Tapken. "Analyse und Synthese akustischer Interaktionsmoden von Turbomaschinen". Dissertation. Berlin, Deutschland: Technische Universität Berlin, 2016.

[11] U. Tapken, B. Pardowitz, and M. Behn. "Radial mode analysis of fan broadband noise". In: *21st AIAA/CEAS Aeroacoustics Conference*. Dallas, Texas (USA), June 2017, AIAA 2017–3715.

[12] J. M. Tyler and T. G. Sofrin. "Axial Flow Compressor Noise Studies". In: *SAE Technical Paper*. SAE International, Jan. 1962.